ELSEVIER

Contents lists available at ScienceDirect

Chemical Engineering Journal

journal homepage: www.elsevier.com/locate/cej





The porous system of a reverse osmosis membrane — operando studies with small-angle neutron scattering

Vitaliy Pipich^a, Thomas Starc^b, Roni Kasher^c, Winfried Petry^d, Yoram Oren^c, Dietmar Schwahn^{b,*}

- ^a Jülich Centre for Neutron Science (JCNS) at Heinz Maier-Leibnitz Zentrum (MLZ), Forschungszentrum Jülich GmbH, D-85747 Garching, Germany
- b Forschungszentrum Jülich GmbH, JCNS-1/ICS-1: Neutron Scattering and Soft Matter, D-52425 Jülich, Germany
- ^c Ben-Gurion University of the Negev, Zuckerberg Institute for Water Research, Jacob Blaustein Institutes for Desert Research, Sede Boker Campus 84990, Israel
- ^d Technische Universität München, Heinz Maier-Leibnitz-Zentrum (MLZ), Lichtenbergstr. 1, D-85748 Garching, Germany

ARTICLE INFO

Keywords: Thin layer composite RO membranes Pore structure Supporting layers Operando small-angle neutron scattering

ABSTRACT

This manuscript deals with operando small-angle neutron scattering (SANS) on a reverse osmosis (RO) thin film composite (TFC) membrane, which was exposed to salt-free water at a transmembrane pressure of 25 bar and a transverse flow rate of 18 L/h. Permeate flux and electric conductivity were detected in parallel to SANS. The relevant objects of investigation are macro- and nanopores in the range of μm and n m, which were investigated with two SANS diffractometers covering a scattering vector \underline{Q} between 10^{-4} and $0.3~\text{Å}^{-1}$. Salt-free water isotopes of H_2O and D_2O and their mixtures were used for the purpose of contrast matching, thereby determining the size of pores in the membrane layers. Macropores of the order of μm dimension were found in the nonwoven polypropylen (PP) layer showing a decline in size between 2 and 2.5 % over the experimental time of 7 to 17 h. The macropores of the polysulfone layer (PSU) have a size of about 0.4 μm . Nanopores with an average total diameter of $(23.7 \pm 0.5)~\text{Å}$ of volume fraction of the order of 2 % vol are found exclusively in the PSU layer. The pore morphology was compared with the results of local methods such as SEM and TEM tomography, showing the complementarity of these methods and their necessity for a more complete picture of membrane morphology. A correlation between permeate flux and SANS parameter is discussed.

1. Introduction

It is claimed by UNICEF that "everyone has the right to safe drinking water". To meet this demand for regions with small fresh water sources, drinking water is obtained primarily from seawater, brackish water, and wastewater. Today, the major technology for desalinating water is reverse osmosis (RO), which is a pressure-driven process [1]. This technique is rather complex with respect to: (i.) the design of RO membranes in particular with respect to the pore structure of the selective polyamide (PA) layer of thin film composite (TFC) membranes, (ii.) the transport process of water and salt molecules through the membrane, as well as (iii.) mineral scaling and organic fouling on the membrane surface [2–4].

Small-angle neutron scattering (SANS) is an ideally suited technique for the investigation of RO processes. SANS does not require complex sample preparation, is non-destructive and allows the characterization of the relevant pore structure of TFC membranes from microscopic (µm)

to nanoscopic (nm) dimensions, and the parameters obtained represent ensemble averages over a volume of typically 0.1 to 1 mL. These properties give hope for interesting information from time-resolved operando studies, such as the development of membrane pores, scaling and fouling of crystalline or organic compounds on the membrane surface.

A review of "Advanced Characterization in Clean Water Technologies" such as neutron scattering is found in ref. [5]. Our fundamental goal is to better understand the process of mineral deposition of calcium phosphate (Ca₃(PO₄)₂) and calcium carbonate (CaCO₃) and their interaction with organic molecules on the membrane surface. First published work was in vitro SANS experiments [6–8], showing a close connection to biomineralization such as precipitation of Ca₃(PO₄)₂ in biological fluids [9,10]. We further used SANS and positron annihilation lifetime spectroscopy (PALS) to analyze the pore structure of several commercial polyamide (PA) thin-film composite (TFC) membranes [11] as well as of standalone polyamide layers [12] to better understand the characteristic scattering patterns of these multilayer RO membranes. This information

E-mail address: d.schwahn@fz-juelich.de (D. Schwahn).

^{*} Corresponding author.

is relevant by itself but also important for later analysis of scaling and fouling layers. For these experiments, we have developed an operando device to simulate the process of salt and wastewater desalination with SANS. Such a device can be realized because most materials are transparent (i.e., have a small absorption cross section) to neutrons. First experiments were published in [13] using a prototype equipment, whereas the full developed device became available for experiments on silica dispersions [14]. Two pressure cells were installed in a feed circuit, one with a membrane (RO-MC) and the other without a membrane (RO-EC). In the RO-EC cell, only the feed was measured directly after leaving the membrane cell. The SANS data from the RO-EC cell is important to verify the purity of the water in terms of dissolved molecules. In parallel with the SANS data, the permeate flux of the membrane and the electrical conductivity of the feed solution were determined for comparison with the relevant parameters of the membrane structure. Section 4 (Summary and Discussion) also compares the microscopic pore morphology from SANS with results of local methods such as SEM and TEM tomography from the literature, demonstrating the complementarity of these methods and their necessity for a more complete picture of membrane morphology.

The present manuscript deals with SANS studies on a RO membrane exposed to salt-free water. These experiments are generally performed as part of a standard procedure for cleaning and compaction of pristine membranes prior to desalination studies. A review on pretreatment technologies on reverse osmosis is found in ref. [15]. The operando experiments performed with two SANS instruments, covering the range from µm to nm, allow the investigation of the changes in the porous structures associated with the two support layers of the selective polyamide layer of any TFC-RO membrane. Although the current study does not cover the sub-nm region associated with the pores of the selective polyamide layer, it is of great importance for elucidating the effects of the other structural components on the overall performance of the TFC-RO membranes. In this context, it is important to emphasize that it is now known that the performance of the selective polyamide layer of TFC membranes is strongly influenced by the chemical and porous structure of the support layers [16–19].

2. Material and methods

2.1. SANS instruments and reverse osmose equipment

The neutron experiments were performed at two SANS instruments, both operating at the MLZ (Heinz Maier-Leibnitz Zentrum) of the FRM II research neutron source in Garching, Germany [20], covering a scattering vector Q of magnitude from 10⁻⁴ to 0.3 Å⁻¹, thereby allowing the analysis of scattering particles from nm to µm size. The experiments were performed at the KWS1 and KWS3 instruments. KWS3 is an instrument for "very-small" angle scattering (VSANS) by the use of a focusing mirror for neutrons, covering a Q range from 10^{-4} to 2×10^{-3} $Å^{-1}$ whereas KWS1 is a classical pin-hole instrument covering a Q range from 2×10^{-3} to 0.3 Å⁻¹ [21,22]. A recent overview about the current status of SANS technique is given by Barker et al. in ref. [23]. The magnitude of Q is determined according to $|Q|=4\pi/\lambda\sin(\delta/2)$ from scattering angle δ and neutron wavelength λ and is related to the inverse size $(Q \simeq 2\pi/d)$ of the objects of investigation (d) such as pores. With respect to the objective of this study, KWS3 focusses on macropores in the range of µm diameter, whereas KWS1 covers smaller pores, typically in the nm range. The scattering laws for small-angle neutron scattering and sample parameters needed are summarized in Appendix A.

The apparatus for the operando SANS experiments is described in detail in a recent paper [13,14]. The adjective "operando" means that the process of desalination of RO wastewater is carried out in real time in a neutron beam in a realistic manner that mimics the final purification process to obtain drinking water. As already mentioned, the SANS measurements of membrane and feed were carried out in two pressure

cells installed in the feed circuit, one cell with membrane (the RO-MC cell), the other without membrane (the RO-EC cell), in order to determine the respective scattering of the membrane plus feed and the feed alone. A recent review article covering the full range of neutron scattering application on polymer structures and dynamics has been published by Richter et al. [24].

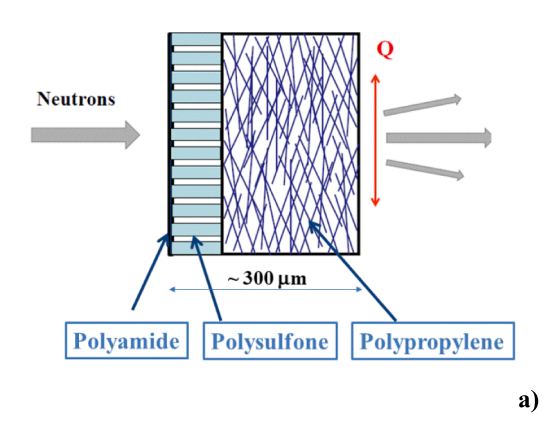
2.2. Membrane and feed solution

The experiments were performed with the polyamide thin film-composite membrane RO98pHt by Alfa Laval [25]. The schematic structure of the TFC membrane of an overall thickness of $\simeq 300~\mu m$ is shown in Fig. 1a along with the directions of the incident and scattered neutron beams. The polymers of the three layers are: active skin layer of an aromatic polyamide (PA) of $\simeq 0.2~\mu m$ thickness, porous support layer of polysulfone (PSU) of $\simeq 40~\mu m$ thickness, and nonwoven layer of polypropylene (PP) of $\simeq 260~\mu m$ thickness (Table A3). To illustrate, the scattering profile of a RO98pHt membrane exposed to deionized (DI) water at ambient conditions is shown in Fig. 1b.

The scattering vector Q of the experiments at KWS1 and KWS3 covers a Q range from $\simeq 10^{-4}$ to $0.3~\text{Å}^{-1}$ thereby being sensitive to pores between several μm and nm size. The scattering pattern of the TFC membrane reveals three scattering centers due to their highly varying dimensions, namely the two larger ones of $\simeq 1.7~\mu m$ and $\simeq 0.4~\mu m$ radius of gyration (Rg), which were attributed to the PP and PSU layers, respectively. The smaller pores of $\simeq 10~\text{Å}$ radius at large Q will be topic of this manuscript showing similar size as found for standalone PA layers in ref. [12]. An extensive morphological analysis of several commercial TFC membranes was carried out by us under the application of SANS contrast variation and positron-annihilation lifetime spectroscopy in ref. [11]. The contrast experiments were performed with D2O/H2O isotope mixtures and supercritical CO2 fluid varying, respectively, composition, temperature and pressure. Recent SANS research on supercritical CO2 has been published in [26,27].

For small angles the strength of neutron scattering intensity of given particles dissolved in a solvent is determined by $\Delta \rho^2 = (\rho_P - \rho_S)^2$ the square of the difference between the coherent scattering length densities of the particles, in our case the membrane polymers (ρ_P) and the solvent water (ρ_w) , which we call scattering contrast. The coherent scattering length density of water (ρ_S) has different values for H₂O and D₂O, namely $\rho_{H_2O}=$ -0.508 and $\rho_{D_2O}=$ 6.384 in units of 10¹⁰ cm⁻² (Table A2) through the interaction of neutrons with the nuclei of hydrogen and deuterium atoms. Assuming the solvent water penetrates into the pores of the membrane those become visible with different contrast for D₂0, H₂O or mixtures of both. This property is the basis of neutron contrast variation widely applied in neutron scattering [23,24] as in this manuscript to identify the pores in the individual layers of the RO membrane. An example of scattering of the RO98pHt membrane exposed to H₂O, D₂O and a 50 % mixture of H₂O/D₂O is shown in Fig. A1a and in the graphical abstract. The corresponding scattering contrasts (i.e. $\Delta \rho^2 =$ $(\rho_P - \rho_W)^2$) of the membrane polymers have been compiled in Table A3 and depicted in Fig. A1b (top) against D₂O content in Appendix A. Fig. A1b (bottom) shows the corresponding $D_S \times \Delta \rho^2$ (also listed in Table A3), which is the more relevant parameter for comparing the scattering power of the individual membrane layers of different thickness D_s as seen from the scattered neutron intensity $\Delta I_D(Q)$ in Eq. (A2). The parameter $D_S \times \Delta I_D(Q)$ has the meaning of a scattering probability. Fig. A1b shows that the PSU and PP layers dominate the scattering for all aqueous solutions of the D₂O/H₂O mixture. In this discussion we neglected the effect of volume (V_P) and formfactor (F(Q)) whose amplitude and shape are determined by the size of the pores as seen in Eqs. (A4) and (A5).

The PSU layer shows zero scattering contrast in a water mixture of 38 % vol D₂O content, whereas the PP nonwoven layer has nearly zero contrast in H₂O (zero scattering for 3.3 % vol D₂O content), it strongly



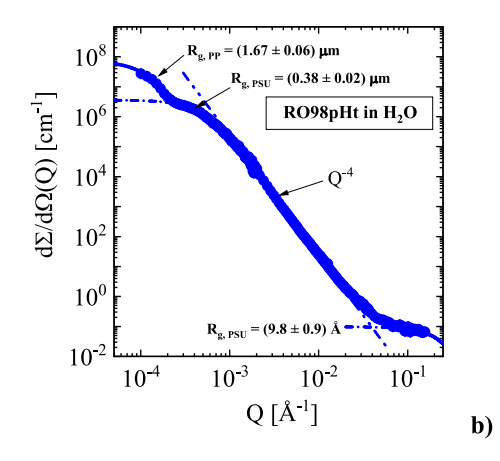


Fig. 1. A) Schematic design of the RO thin film composite membrane used in the neutron scattering experiments. b) Scattering curve of a RO98pHt membrane at ambient conditions exposed to deionized water (H_2O). Scattering from pores of three different sizes becomes visible. The two larger pores were identified as part of PP and PSU support layers [11]. In this paper (Fig. 13), nanopores of $\simeq 10$ Å radius were identified as part of the PSU layer.

increases with D_2O concentration to the dominating scattering contrast of the membrane. The degree of scattering of the PA skin layer is too small (orders of magnitude smaller than the PSU and PP layers) to contribute a measurable signal because of its significantly smaller thickness of $\simeq 0.2$ mm. However, a measurable signal from PA pores might become visible at the large $Q>0.1~\mbox{\normalfont\AA}^{-1}$ as shown in Fig. 1b, when scattering of $R_g \simeq 10~\mbox{\normalfont\AA}$ pores becomes visible, which as well might be attributed to the PSU layer.

The experiments of this study were performed with the membrane RO98pHt at 25 bar and CF = 18 L/h cross-flow. We studied several saltfree isotope D₂O/H₂O mixtures of various D₂O contents as feed usually applied for membrane compaction before starting desalination. Before starting experiment, the membrane samples were prepared as follows: (i.) Cutting out a membrane to $15.5 \times 6 \text{ cm}^2$ and glue it watertight into a metal frame of the pressure cell (RO-MC). The active area of the membrane is about 40 cm². (ii.) Cleaning the membrane for nearly 20 h in 40 % aqueous isopropanol solution, and (iii.) rinsing the membrane between 2 and 4 h with deionized water (H₂O). In case of experiments with an isotope mixture of D₂O/H₂O we applied the same mixture, i.e. same volume fractions (Φ and (1- Φ)) of D₂O and H₂O for the cleaning process. This treatment of commercially available membranes is a common practice aimed at removing some of the preservatives added by manufacturers, such as glycerine. In all tests, the porous structure of the pretreated membrane is taken as the starting point. The pre-treatment does not cause any damage to the membrane structure.

3. Results: Membrane exposure to salt-free water

Prior to the experiment, the pristine membrane was compacted in order to obtain the appropriate pore structure and thickness at the specific operational conditions. In parallel to the SANS experiments, the electric conductivity (EC) of the feed and permeate were determined. The electrical conductivity (EC) measured within the closed circuit of the feed water [14] always showed a continuous increase in the EC value, although we always started our experiments with salt-free water, as shown in this section. The possible reasons for the conductivity changes are discussed in section 4.3. The RO98pHt reverse osmosis membrane has the advantage of low neutron scattering contrast of the polypropylene (PP) nonwoven layer in H_2O and thus an order of magnitude lower coherent scattering signal compared to the porous PSU support layer, as shown in Fig. A1b and summarized in Table A3.

This section is divided into two chapters of experiments performed by SANS: the first one about the detection of macropores in the supporting layers, done with KWS3. The second section focuses on the detection of nanopores by KWS1. Common to all experiments is the usage of contrast variation by different isotopic mixtures of $\Phi/(1-\Phi)$

 D_2O/H_2O exposed to the membrane for more information about the location of the pores [11].

3.1. Macroporous structure of RO membranes in salt-free water

Macropores are part of the structure of the PSU and PP layers. The scattered intensity of the membrane cell RO-MC was normalized to the total thickness (D_S) of the membrane of 300 μm (Table A1). Parameters of the PSU (\simeq 40 μm) and PP (\simeq 260 μm) layers will be renormalized later with their corresponding thickness. The thickness of the PSU layer was estimated according literature between 40 and 50 μm . Scattering from the PA selective skin layer is negligible from its "ultra" small thickness of the order of 0.2 μm (Table A3). Experiments are shown with feeds of D₂O, H₂O, and a 50:50 D₂O/H₂O mixture.

3.1.1. Membrane macropores exposed to D_2O

The permeate flux and electrical conductivity (EC) of D_2O feedwater exposed to *a pristine membrane* are shown in Fig. 2a for a run time of 18 h at 25 bar and cross flow of 18 L/h. The permeate flux decreases by about 30 % from 27 to 18 L/m²h following an exponential decrease with a time constant of about 12 h.

In parallel, the electrical conductivity (EC) increases by a factor of almost 3 from 20 to 54 $\mu S/cm$, first increasing linearly with a slope of (2.61 \pm 0.01) $\mu S/(cmh)$ and after 6.9 h with a slower rate of (1.49 \pm 0.01) $\mu S/(cmh)$, showing a small degree of feed contamination. This result is surprising as the EC of salt-free water is expected to be small in the range of some 10 $\mu S/cm$ but constant in time. Fig. 2b shows the total macroscopic cross-section (Σ_{SANS}) of the membrane cell (RO-MC). Likewise, the electrical conductivity (EC), a two-stage process can be observed: An exponential increase is followed by a slight decrease to a constant value of $\Sigma_{SANS}=$ (88.70 \pm 0.05) cm $^{-1}$ after 6.5 h. Both observations indicate a sensitivity of both parameters to the formation of impurities, which also affect the permeate flux.

The total scattering Σ_{SANS} is derived from the transmission (T) of the primary neutron intensity (i.e. the reduction of the neutron beam in forward direction by neutron absorption and scattering) and sample thickness (D_S) according to $\Sigma_{SANS} = -\ln(T)/D_S$. The "total" macroscopic cross-section represents the integrated scattered neutrons over the space angle according to $\Sigma_{SANS} = \int_{4\pi} d\Sigma/d\Omega(Q) \, d\Omega$, which in case of isotropic scattering becomes expressed as $\Sigma_{SANS} \propto \Phi_P \, (1-\Phi_P) \, l_C$ (Eq. (A10)) with the porous volume fraction Φ_P and the so-called correlation length l_C of the scattering particles as derived in [28–30]. The correlation length represents an averaged value over the pores of the membrane including scaling and fouling particles formed at the PA surface layer. In this sense, similar to permeate flux, Σ_{SANS} can be considered as an integral parameter of the membrane structure.

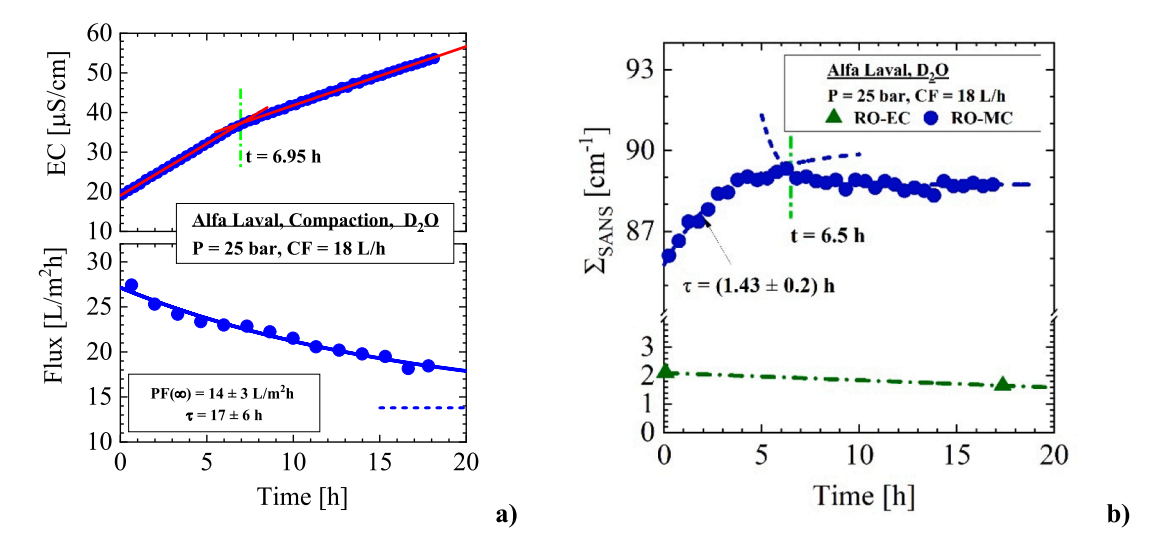


Fig. 2. A) Permeate flux and electric conductivity (EC) measured the feed water in parallel to SANS. After about 7 h, the EC data show a smaller increase in contamination of the salt-free water. The permeate flux is decribed by an exponential decline. No equilibration is observed. b) The total scattering (Σ_{SANS}) of the membrane shows a similar two-step process as the electrical conductivity before and after 6.5 h. The Σ_{SANS} of the RO-EC cell was determined only at the beginning and at the end of the experiment and shows a slight decrease.

Figs. 3a shows the corresponding differential scattering crosssections of the membrane averaged over experimental time. Both membrane layers (PP and PSU) show strong scattering and can be well separated as shown by the dashed-dotted and dashed lines. Such observation was expected from the different pore size and scattering contrast of the PP and PSU layers as, respectively, evaluated from the

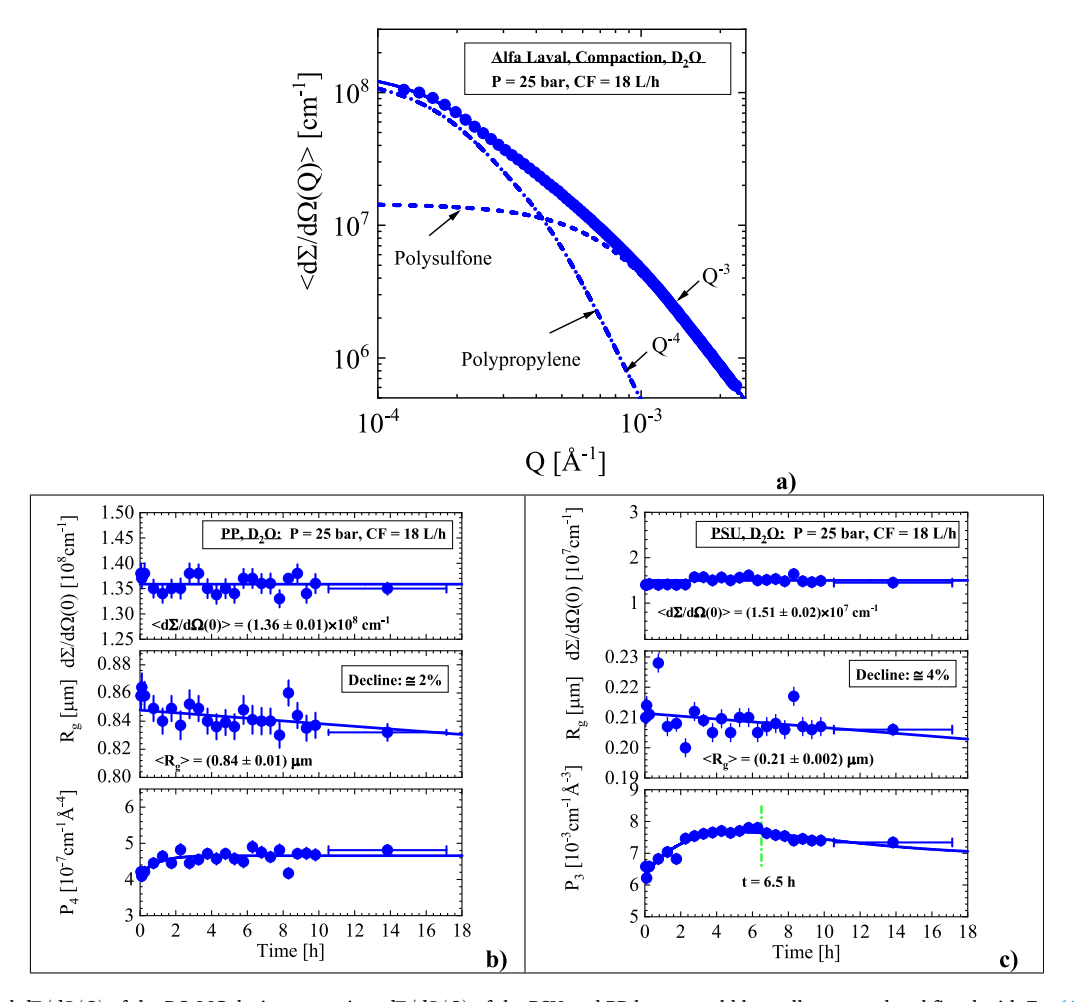


Fig. 3. A) Averaged $d\Sigma/d\Omega(Q)$ of the RO-MC during operation. $d\Sigma/d\Omega(Q)$ of the PSU and PP layers could be well separated and fitted with Eq. (A6) as indicated by the two lines. b-c) Parameters from fitting show only minor changes of pore size and surface, the latter one determined from the Porod constants P₄ and P₃ (Eq. (A8)).

parameters as = 1.13 and 0.093 in units of 10^{20} cm⁻³ in Table A3. The SANS parameters in Fig. 3b and c are constant or slightly changing with time. Both pore radii (R_g) show slight decline of about 2 % and 4 % for the PP and PSU layer, respectively. On the other hand, the pore surface slightly increases as determined from the Porod constants (Eq. (A8)). This is a signature of an evolution of the pores towards a more ellipsoidal shape with a larger surface area. In particular, the parameter P_3 of the PSU layer (Fig. 3c) shows qualitatively a similar profile as in Fig. 2b, namely a small hump at 6.5 h after a continuously increase of 23 % followed by a slight decline of 10 %.

3.1.2. Membrane macropores exposed to H_2O

The experiment with salt-free H₂O was performed with the *same membrane sample of the previous D*₂O *experiment* after careful cleaning of the RO-MC and RO-EC cells including the feed circuit with DI-H₂O. The contrast of the membrane layers soaked in H₂O is almost zero for the PP nonwoven layer and sufficiently good for the PSU porous support layer (Fig. A1b). This implies that the scattering of the PP nonwoven layer is sufficiently reduced that the scattering of the PSU layer can be explored with better precision as visualized in Fig. 1b. Quantitatively, this means that $D_S \times \Delta \rho^2 = D_S \times (\rho_P - \rho_{H_2O})^2$ of the membrane layers PSU and PP is 3.49×10^{-2} and 1.39×10^{-3} in units of 10^{20} cm⁻³ (Table A3), i.e. the scattering contrast times thickness of the sample $D_S \times \Delta \rho^2$ of the PSU support layer is $\simeq 25$ times larger.

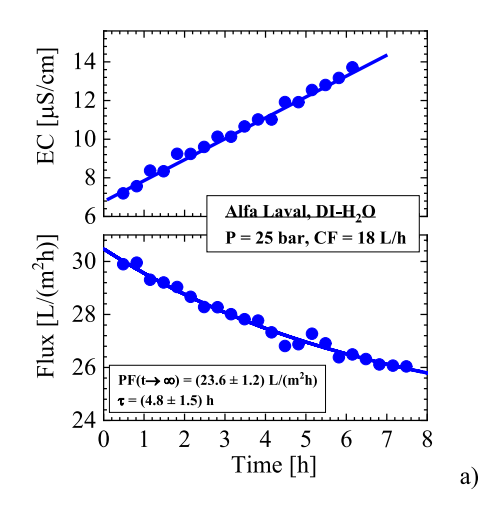
Fig. 4 shows the electric conductivity (EC) of the feed and the permeate flux when exposed to the salt-free water H₂O at a pressure of 25 bar and cross-flow of 18 L/h. The EC increases linearly from about 7 to 14 μ S/cm, whereas the permeate flux declines from \simeq 30 to 26 L/ (m²h) to a level of 87 % following an exponential decline with a time constant of about 5 h. Fig. 4b shows the corresponding total macroscopic cross-section (Σ_{SANS}), the increase of which relaxes exponentially with a time constant of (5.3 \pm 1.1) h in a similar way, as the permeate flow decreases throughout the experimental time of 8 h. The permeate flux of H₂O is slightly larger than for D₂O (Fig. 2) but shows a much smaller relaxation time. On the other hand, Σ_{SANS} increases continuously with a single time constant in contrast to the former D₂O experiment in Fig. 2. This in turn means that individual molecules and/or aggregates continue to detach from the membrane, albeit in a smaller extent than the previous 18-hour D₂O experiment. On the other hand, Σ_{SANS} of the empty cell (RO-EC) shows several orders of magnitude smaller values with weak increase.

Fitting the differential cross-section $d\Sigma/d\Omega(Q)$ in Fig. 5a allows more detailed information about the PSU and PP membrane layers to be obtained, as shown in Fig. 5b - d. The polypropylene (PP) layer in Fig. 5b

shows a slight decrease in pore size of about 2.5 % in consistence with the D₂O experiment and about a 10 % decline of $d\Sigma/d\Omega(Q=0)$. On the other hand, the PSU layer shows a remarkable increase in scattering, as can be seen in Fig. 5a delivering a Q^{-3} power law at large Q (i.e. $Q \times R \ge$ 1), which points to a mass fractal exponent [28] (p. 189). Fig. 5c and d show the relevant parameters of the PSU layer. The pore size R_g stays constant with an average value of < R_g> = (0.38 \pm 0.01) μ m, whereas $d\Sigma/d\Omega(0)$ and the amplitude of the Q^{-3} power law P₃ both increase by a factor of 1.96 and 2.2, respectively. P3 in Fig. 5d shows a linear increase for the first 3 h, which afterwards changes to a more exponential increase. We can relate the increase of both parameters of scattering intensity to the process of filling the pores with water. The degree of filling with H₂O can be estimated as follows: The PSU layer has a scattering length density of $\rho(PSU) = 2.08 \, \times \, 10^{10} \text{ cm}^{-2}, \text{ whereas } H_2O \text{ has a}$ negative $\rho(H_2O) = -0.561 \times 10^{10}$ cm⁻² (Table A2), i.e. filling the PSU pores with H₂O increases the scattering contrast of the pores according to $\delta \rho(PSU) = [\rho(PSU) - \rho(H_2O)] = 2.641 \times 10^{10} \text{ cm}^{-2}$. The maximum possible increase of scattering intensity is determined by the square of the ratio of $[\rho(PSU) - \rho(H_2O)]/\rho(PSU)$ giving an enhancement factor of 1.61 as has been visualized by the black arrow in Fig. 5e. This value is lower than the two measured enhancement factors of $d\Sigma/d\Omega(0)$ (18 %) and P₃ (27 %) after 7 h treatment visualized by the red and green arrows in Fig. 5e, i.e. we can assume that the pores were completely filled with H₂O. However, it must be considered that this membrane was previously exposed to D₂O, as described in the previous section. We therefore may assume that there is still a residue of D₂O in the pores of the PSU layer. This means that an exchange of D₂O with H₂O in the pores of the PSU layer could also lead to an increase in intensity, as quantitatively explained in Fig. 5e. An important argument for this scenario, besides the stronger increase of the scattering intensity, could be the long duration (7 h) of this process without signs of saturation. The absence of saturation suggests an even higher D2O content of the water in the PSU macropores at the beginning of the experiment.

3.1.3. Membrane macropores exposed to $50/50\ D_2O/H_2O$

A *pristine membrane* was implemented into the RO-MC for this cell experiment. A salt-free mixture of 50/50 D₂O/H₂O exposed to the membrane allows the PP nonwoven layer to play the dominant role in scattering (Fig. A1b). Quantitatively, this means that $D_S \times \Delta \rho^2 = (\rho_P - \rho_W)^2$ of the PP and PSU membrane layers are respectively 2.63 × 10^{-1} and 3.49×10^{-3} in units of 10^{20} cm⁻³ (Table A3), i.e., the scattering contrast time sample thickness of the PP nonwoven layer is 75 times larger (Fig. A1b, bottom). However, the large difference in pore size, which is of the order of 1 and 0.3 μ m leads to a ratio of pore volume (Eq.



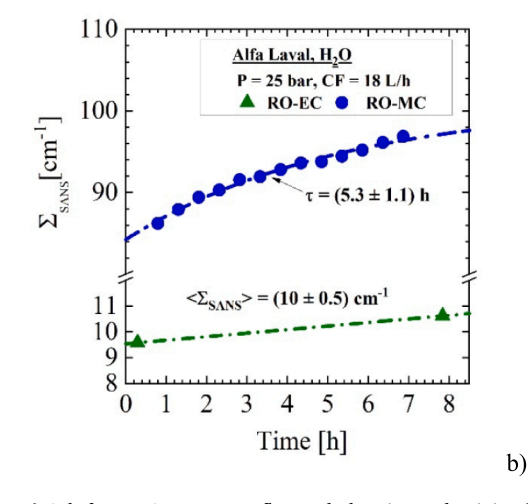


Fig. 4. Same membrane from previous D_2O experiment after careful cleaning. a) Salt-free H_2O : Permeate flux and electric conductivity (EC) as well as b) total macroscopic cross-section Σ_{SANS} from membrane (RO-MC) and empty (RO-EC).

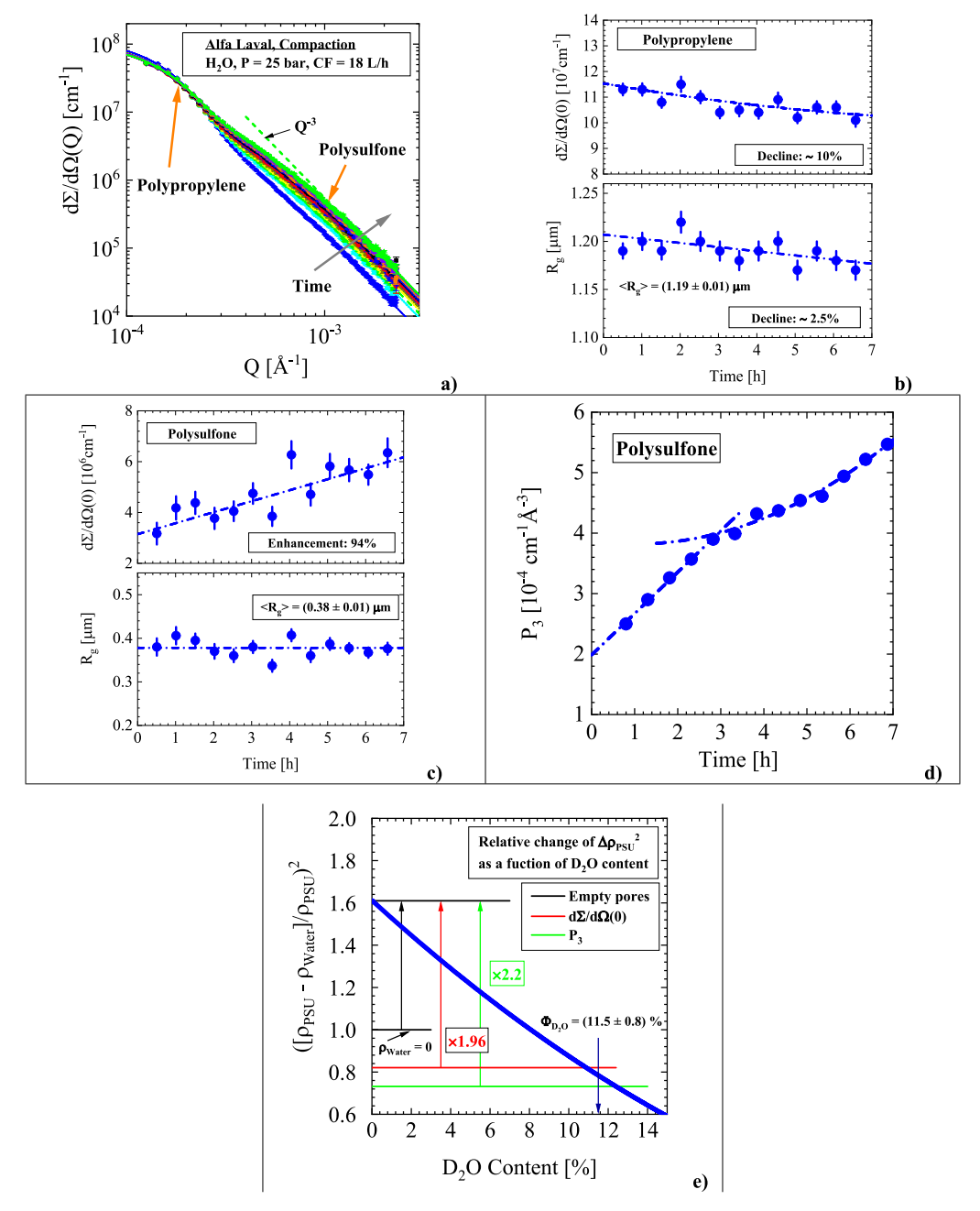


Fig. 5. A) Scattering data of the membrane exposed to salt-free H_2O . The arrow shows the direction of the development of the scattering of the PSU layer expressed by the parameter P_3 in d). b) to d) show parameters from the PP and PSU layers. e) Relative change in PSU scattering contrast versus D_2O content of the macropores (PSU) at the beginning of the experiment.

(A4)) of the order of 40 and therefore for a further increase to 3×10^3 for the $d\Sigma/d\Omega(0)$ of the PP layer. However, this large factor is partially compensated at larger Q by the shape factor (Eq. (A5)), as it can be estimated by Guinier's law (first term of Eq. (A6) according to $\exp{[-(R_gQ)^2/3]}$; a decrease of $\simeq 5\times 10^{-4}$ is obtained for $Q=5\times 10^{-4}$ Å $^{-1}$, i.e., a factor of 1.5, which allows a separate analysis of the PP and PSU scattering (Fig. 1b and 7a).

Fig. 6a shows permeate flux and electric conductivity of the salt-free water in the feed circle. At the beginning, the electrical conductivity already has a value of about $27~\mu S/cm$ compared to 18 and $7~\mu S/cm$ for the individual components D₂O and H₂O (Fig. 2a and 4a) and increases over the course of 7 or 20 operating hours by $2~\mu S/cm$ and $5~\mu S/cm$.

The permeate flux is almost half that of H_2O (Fig. 4) and falls exponentially to about 60 % after 20 h of treatment. Fig. 6b shows the

corresponding Σ_{SANS} determined from the transmission of membrane (RO-MC) and empty cell (RO-EC). The RO-MC shows an exponential increase of $\simeq 14$ % with a time constant of $\tau \simeq 4$ h and an amplitude about half of the corresponding H₂O one. The cross-section Σ_{SANS} of the isotope mixture (RO-EC) decreases with an amplitude of (1.95 \pm 0.05) cm⁻¹ or by 23 % with a time constant of almost 4 hrs. Later in this section it will become clear that the change of Σ_{SANS} is due to an increase of the D₂O content from 38 % to 50 % of the isotope mixture (Fig. 11), which corresponds to a decline of incoherent scattering cross-section (Table 1) from 19 % to slightly smaller than 23 %.

The scattering data of the membrane are depicted in Fig. 7. Fig. 7a shows two scattering curves at times after 3.3 and 19.3 h of operation showing the PP layer as the expected dominant one. The PSU part, extracted as dashed dotted lines from $d\Sigma/d\Omega(Q)$, is several orders of

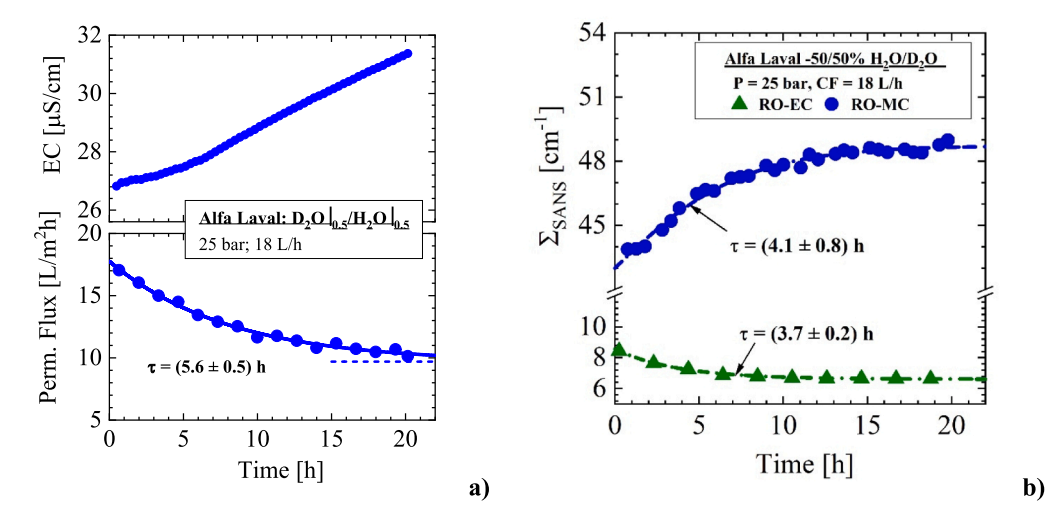


Fig. 6. Membrane exposed to the isotope mixture of nominal $0.5/0.5~D_2O/H_2O$ salt-free water. a) The electric conductivity and permeate flux and b) the total scattering cross-section from membrane and feed solution. The time constant (τ) of Σ_{SANS} equal to 4.1 h is slightly smaller than $\tau=5.6$ h of the permeate flux.

Table 1
Parameters of nanopores. The SANS data of $\Phi_p(D_2O) = 22$ and 72 % vol are not shown. The values of $d\Sigma/d\Omega_{inc}$ for H_2O and D_2O were evaluated from the incoherent cross sections tabulated in [33] (p. 67 Table 5), see also discussions in [32]. The other SANS parameters were normalized to the cell thickness of 0.172 cm at 25 bar (Table A1).

Condition	Parameter	H ₂ O	22:78 D ₂ O/H ₂ O	60:40 D ₂ O/H ₂ O	72:26 D ₂ O/H ₂ O	D_2O
Calculated	$d\Sigma/d\Omega_{inc} [cm^{-1}]$	0.446	0.353	0.185	0.133	1.11 × 10 ⁻²
P = 25 bar CF = 18 L/h	$d\Sigma/d\Omega_{Backr.}$: RO-MC [cm ⁻¹]	0.863 ± 0.003	0.691 ± 0.001	0.416 ± 0.006	0.313 ± 0.002	$(7.28 \pm 0.02) \times 10^{-2}$
	$d\Sigma/d\Omega_{Backr.}$: RO-EC [cm ⁻¹]	0.80 ± 0.01		0.344 ± 0.001	0.238 ± 0.002	$(3.05 \pm 0.01) \times 10^{-2}$
	P ₄ [10 ⁻⁷ cm ⁻¹ Å ⁻⁴]	0.984 ± 0.004	0.144 ± 0.008	0.199 ± 0.002	0.583 ± 0.003	2.01 ± 0.01
	$d\Sigma/d\Omega(0)$ $[10^{-3} cm^{-1}]$	2.92 ± 0.14	1.38 ± 0.38	1.35 ± 0.47	2.33 ± 0.20	3.95 ± 0.06
	R _g [Å]	9.18 ± 0.17	9 (fixed)	9.1 ± 0.6	7.34 ± 1.4	7.92 ± 0.12
	$ m Q2 \ [10^{-5} \ cm^{-1} \ \AA^{-3}]$	0.827 (t = 20 h)	about zero	0.22 (t = 13.5 h))		1.64 (t = 35 h)

magnitude smaller at Q = 0 and increases during operation by two orders of magnitude as seen in Fig. 7a and b. During the first 3 h we observe a slight decline of intensity to nearly 4×10^3 cm⁻¹, which is too small for further analysis (straight dashed-dotted line in Fig. 7a). In the further course of operation, we observe an increase of intensity, first quadratic and then exponentially achieving a value of $\simeq 3.7 \times 10^5 \, \text{cm}^{-1}$ after 20 h of treatment (dashed-dotted line in Fig. 7a and b). The minimum of $d\Sigma/d\Omega(Q=0)$ at 2.6 h represents the matching point of the PSU layer with the isotope mixture thereby giving the clear indication of a 38 % vol D₂O feed concentration at that time as evaluated from the equivalence of coherent scattering lengths density of the PSU polymer and the molecules of the isotope mixture of water (Table A2), i.e. $\rho_{PSU}=$ $\rho_{Water}(\Phi_{D_2O}=0.38)=2.08\times10^{10}\,\mathrm{cm}^{-2}.$ This D₂O concentration is much below the nominal D₂O concentration of 50 % vol. Subsequently, $d\Sigma/d\Omega(Q=0)$ of the PSU layer increases continuously caused from growing D2O concentration in the D2O/H2O mixture towards its nominal value.

The increase in D_2O concentration is naturally visible to the PP layer as well, as shown in Fig. 7c. A slight increase in $d\Sigma/d\Omega(0)$ and a larger increase in P_4 can be seen, although the pore size decreases by 9.3 %, corresponding to a 25 % decrease in pore volume. A parameter for further analysis and cross check is the second moment Q_2 in Fig. 7d, as it is an integral parameter only depending on pore volume fraction and scattering contrast (Eq. (A9)). Assuming a constant PP membrane pore volume fraction the observed increase of Q_2 (6.3/3.5 = 1.8) is equivalent to an increase of the scattering length density difference ($\Delta\rho$) of 34

%. Combining $\rho(PP)=-0.325\times 10^{10}$ cm $^{-2}$ with $\rho(38\%D_2O)=2.08\times 10^{10}$ cm $^{-2}$ (Table A2) we get a $\Delta\rho=2.405\times 10^{10}$ cm $^{-2}$, which after multiplication with 1.34 gives a $\rho(49.8\%D_2O)=2.90\times 10^{10}$ cm $^{-2}$ corresponding nearly exactly to the nominal D_2O concentration of 50 % vol.

3.2. Nanoporous system of RO membranes exposed to salt-free water

In this section we use the classical pinhole instrument KWS1 [22] for broadening our knowledge to the behavior of pores of the order of 10 Å radius determined from $d\Sigma/d\Omega(Q)$ in the range from 0.1 to 0.3 Å $^{-1}$. This Q range is usually dominated by incoherent scattering whose $d\Sigma/d\Omega_{\rm inc}$ is compiled below in Table 1 for the different isotopic forms of H₂O, D₂O, and mixtures of $\Phi/(1-\Phi)$ D₂O/H₂O·H₂O shows the strongest incoherent scattering, which is usually the dominant contribution in this Q range, because the coherent scattering from the corresponding small scattering centers is usually weak, because of $d\Sigma/d\Omega(0) \propto \Phi_P V_P$, i.e. proportional to volume fraction (Φ_P) and volume (V_P) of the pores (Eq. (A4)). D₂O is the optimal choice for these experiments, as it has (i.) a much weaker incoherent contribution of nearly a factor of 40, and (ii.) – considering the different thickness — has a large coherent scattering contrast particularly for the PSU and PP layers of the membrane (Table A3). Both conditions are relevant for the success of detection of nanopores.

We must mention again the issue of the correct normalization of the membrane cell (RO-MC) in absolute units. Macropores (section 3.1) dominate scattering in the range of $Q = 10^{-4} - 10^{-3} \text{ Å}^{-1}$ by orders of

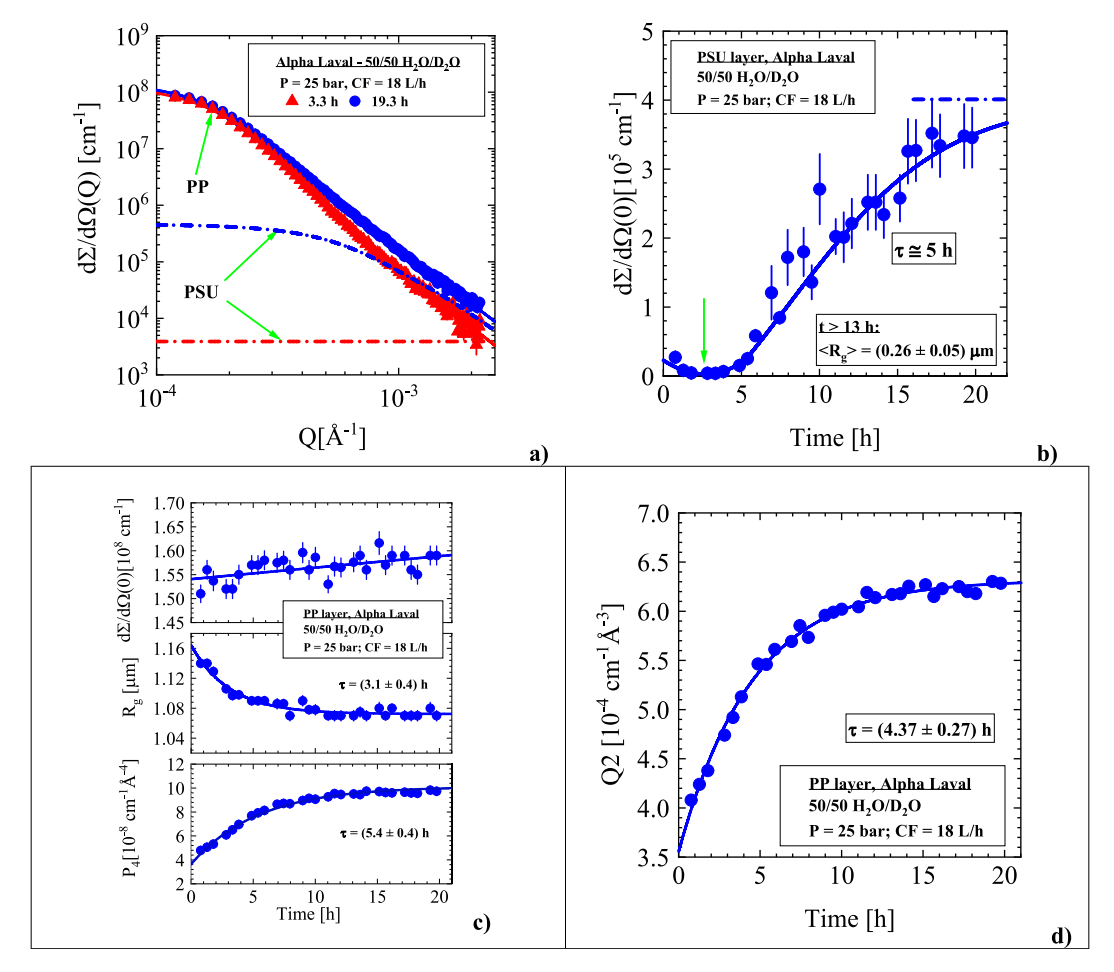


Fig. 7. A) $d\Sigma/d\Omega(Q)$ of nominal 50/50 D_2O/H_2O after exposure of 3.3 and 19.3 h. b) Scattering at Q=0 of PSU layer. The minimum at $t=(2.6\pm0.4)$ h (green arrow) corresponds to the PSU matching condition of $\Phi_{D_2O}=0.38$ (Fig. A1b). The continuous increase of $d\Sigma/d\Omega(0)$ is caused from a change of Φ_{D_2O} from 0.36 in direction to the nominal value of 0.50. c) SANS parameters of the PP layer. The change of Φ_{D_2O} also affects the scattering of the PP nonwoven layer, as can be seen from the overall increase of the intensity parameters as well as in d) of the second moment Q2. (For interpretation of the references to colour in this figure legend, the reader is referred to the web version of this article.)

magnitude and therefore the membrane thickness of 300 μm is the correct value for normalization $d\Sigma/d\Omega(Q).$ However, the situation in the Q range of nanopores from Q=0.1 to $0.3~\textrm{Å}^{-1}$ is different and more complex. The incoherent scattering of water and membrane is measured over the entire cell with a thickness of $D_S=0.172$ cm at 25 bar, while the scattering of nanopores in the PA and PSU layers was normalized to the thickness of the PSU layer with $D_S=40~\mu m$ (Table A1). The thickness of the PA skin layer is reported between 0.1 and 0.3 μm . For this reason, in a first step we normalized $d\Sigma/d\Omega(Q)$ to the sample thickness of $D_S=0.172$ cm and only later corrected the intensity parameters such as $d\Sigma/d\Omega(Q=0)$ and Porod constant P_4 to the thickness of the PSU membrane layer in which the nanopores were identified.

3.2.1. Membrane nanopores exposed to D_2O

Fig. 8 shows the experimental data of a *pristine Alfa Laval membrane* of this section. Fig. 8a compiles permeate flux at a pressure of 25 bar and cross-flow of 14 L/h and the corresponding electric conductivity of the salt-free D_2O over the experimental time of nearly 40 h. The lack of data for permeate flux between 15 and 23 h is due to problems with the inflow of permeate water into the balance. The "salt-free" water tank [14] (Fig. A3) for D_2O was empty and had to be refilled, which is also reflected in the electrical conductivity (EC) data.

The decline of permeate flux is rather strong and looks to fail reaching steady state. In parallel, the EC data show a continuous increase by a factor of 4 from 10 to 40 mS/cm which becomes slower by a factor of $\simeq 7$ after refilling D₂O at 23 h. Fig. 8b shows three scattering

curves: (i.) The RO-EC (green) being completely flat as expected from water, (ii.) two RO-MC curves measured at start (t = 0) (blue) and after 35 h of operation (red). The fitted curves are plotted as solid lines together with their background scattering depicted as dashed dotted lines. Fig. 8c and d show the evolution of background scattering (c) as well as $d\Sigma/d\Omega(0)$ and R_g with time (d). Fig. 8c shows the background for both cells, i.e. RO-EC and RO-MC. In both cases we observe a continuous increase over the first 10 h with same increment of $\delta \simeq 0.65 \times 10^{-2}$ cm $^{-1}$ in both cells, i.e. proving that the water got poisoned with some molecules from the membrane. On the other hand, $d\Sigma/d\Omega(0)$ and R_g in Fig. 8d are rather stable, there is only a slight increase and decline of, respectively, $d\Sigma/d\Omega(0)$ and R_g of 5.3 % and 21 % as determined from the fits of both parameters applying an exponential function. However, the statistical error bars are with 10 % and 5 % relatively large as seen from the error bars in Fig. 8d.

3.2.2. Membrane nanopores exposed to H_2O

Following the previous experiment, devices including the membrane were thoroughly cleaned with deionized H_2O with the result of an electric conductivity (EC) in the μ S/cm range as shown in Fig. 9a. Unlike to the earlier D_2O experiment (Fig. 8a), we observe only a slight increase in EC over the experimental period of 21 h. Accordingly, the permeate flux also shows only a small decrease of $\simeq 10$ % in contrast to $\simeq 35$ % for the D_2O case after 20 h (45 % after 40 h) of operation. The slight increase of permeate flux between 5 and 10 h is due to an adaptation of the transmembrane pressure by $\delta P \simeq 1$ bar. These data show that no more

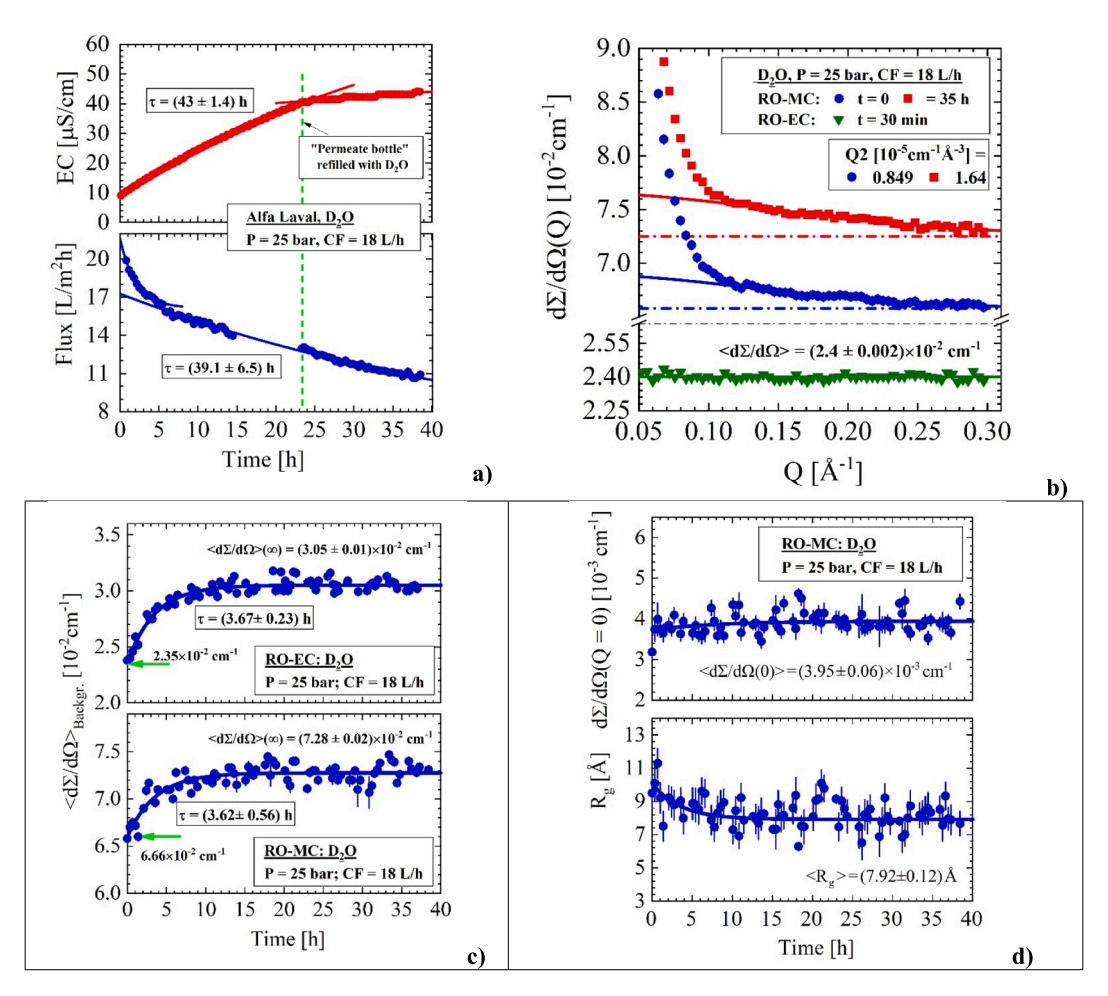


Fig. 8. Collection of salt-free D_2O data: a) Permeate flux and electric conductivity (EC) data for the experimental run of nearly 40 h. After 23 h, the fresh D_2O tank of the pressure piston had to be refilled visible by the afterwards smaller increase of EC. b) Large Q data of empty (RO-EC) and membrane cell (RO-MC) at start and after 35 h of operation. The data were fitted with Guinier's law in the Q range between 0.12 and 0.3 Å⁻¹. Scattering from larger pores is only visible from an upturn at low Q. c) Incoherent background scattering of RO-EC and RO-MC cells. The increment of both scattering curves between zero and large time is with 0.007 and 0.0062 cm⁻¹ in the same range, i.e. caused from molecular impurities dissolved in the water in consistency with EC in a). The difference of scattering at zero time of 0.043 cm⁻¹ is due to incoherent scattering of the membrane. d) Corrected scattering from background at Q = 0 and R_g versus time showing a $\simeq 6$ % increase and $\simeq 20$ % decline, respectively.

molecules were released from the membrane as already indicated in Fig. 8a after refilling the bottle with the feed.

The SANS data are shown in Fig. 9b - e. Fig. 9b shows scattering data of the RO-MC and corresponding RO-EC cells after 16 h treatment. The Q⁻⁴ power (Porod) law of Eq. (A8) depicts the large Q tail from the PSU layer of the membrane, whereas the RO-EC cell shows the flat scattering of water nearly approaching the scattering of the membrane at large Q. Here, we have to comment on the observation of the Q⁻⁴ power law for the PSU layer in Fig. 9b which appears in contradiction to the corresponding Q^{-3} behavior of the KWS3 data in Fig. 5a and 7a. From the above it follows that for Q smaller than 2×10^{-3} Å $^{-1}$ and larger than $2\times$ 10^{-3} Å^{-1} a Q^{-3} and Q^{-4} behavior is found, respectively. This is a typical behavior for fractal structures [28] (pp. 188-193). In a former SANS study, we found for standalone polyamide (PA) films a mass fractal structure of pores of $\simeq 8$ Å radius with the exponent $\alpha_{\rm m} = (3.73 \pm 0.01)$ forming a network of pore channels following a mass density (\widetilde{m}) according to $\widetilde{m}(R) \propto R^{(\alpha_m-3)} = R^{0.73}$, i.e. a reduction of mass density with increasing radius R of a fictitious sphere [31]. In the present case we have the situation of a surface fractal, i.e. a rough surface S(R) in three dimensions showing the relationship $S(R) = S_0 R^{(2-\alpha_S)}$ when α_S between 3 ($\propto R^{-1}$) and 2 ($\propto R^{0}$) delivering according to $d\Sigma/d\Omega(Q)\propto Q^{-(6-\alpha_S)}$ a power law behavior of Q $^{-3}$ and Q $^{-4}$. S₀ represents a smooth surface

area with $\alpha_S = 2$. The pores below $Q \le 2 \times 10^{-3} \text{ Å}^{-1}$ (KWS3, Fig. 5) show a rough surface, which appears smooth for $Q \ge 2 \times 10^{-3} \text{ Å}^{-1}$ (KWS1, Fig. 8b) i.e. for length scales less than (1/Q <) 500 Å. A schematic representation of such transition is shown in ref. [31] (Fig. 8).

Fig. 9c shows a selection of large Q data from membrane and empty cells at 25 bar together with the fitted scattering law (Eq. (A6)) shown as solid line whose parameters are depicted in Fig. 9d and e. The scattering of the "10 Å" particles (nanopores) is clearly visible when comparing with the RO-EC scattering. Fig. 9d shows the pore parameters $d\Sigma/d\Omega(0)$ and R_g versus time. The radius of gyration (R_g) shows the constant value of average (9.18 \pm 0.17) Å, whereas $d\Sigma/d\Omega(0)$ decreases after about 5 h by $\simeq 50$ % from $d\Sigma/d\Omega(0)=5.5\times 10^{-3}~cm^{-1}$ to the average $< d\Sigma/d\Omega$ (0)> $=2.92\times 10^{-3}~cm^{-1}$ indicating a decline either of pore volume fraction or of scattering contrast.

3.2.3. Membrane nanopores exposed to $60/40 D_2O/H_2O$

This section deals with the isotope mixture of nominal 60/40 $D_2O/H_2O.$ Fig. 10a shows the electric conductivity (EC) and permeate flux at 25 bar and 18 L/h cross-flow over the experimental time of 15 h. The EC increases linearly by a factor of 3 from 10 to 30 mS/cm, whereas the permeate flux declines exponentially from 19.6 to 14.5 L/(m^2 h) to \simeq

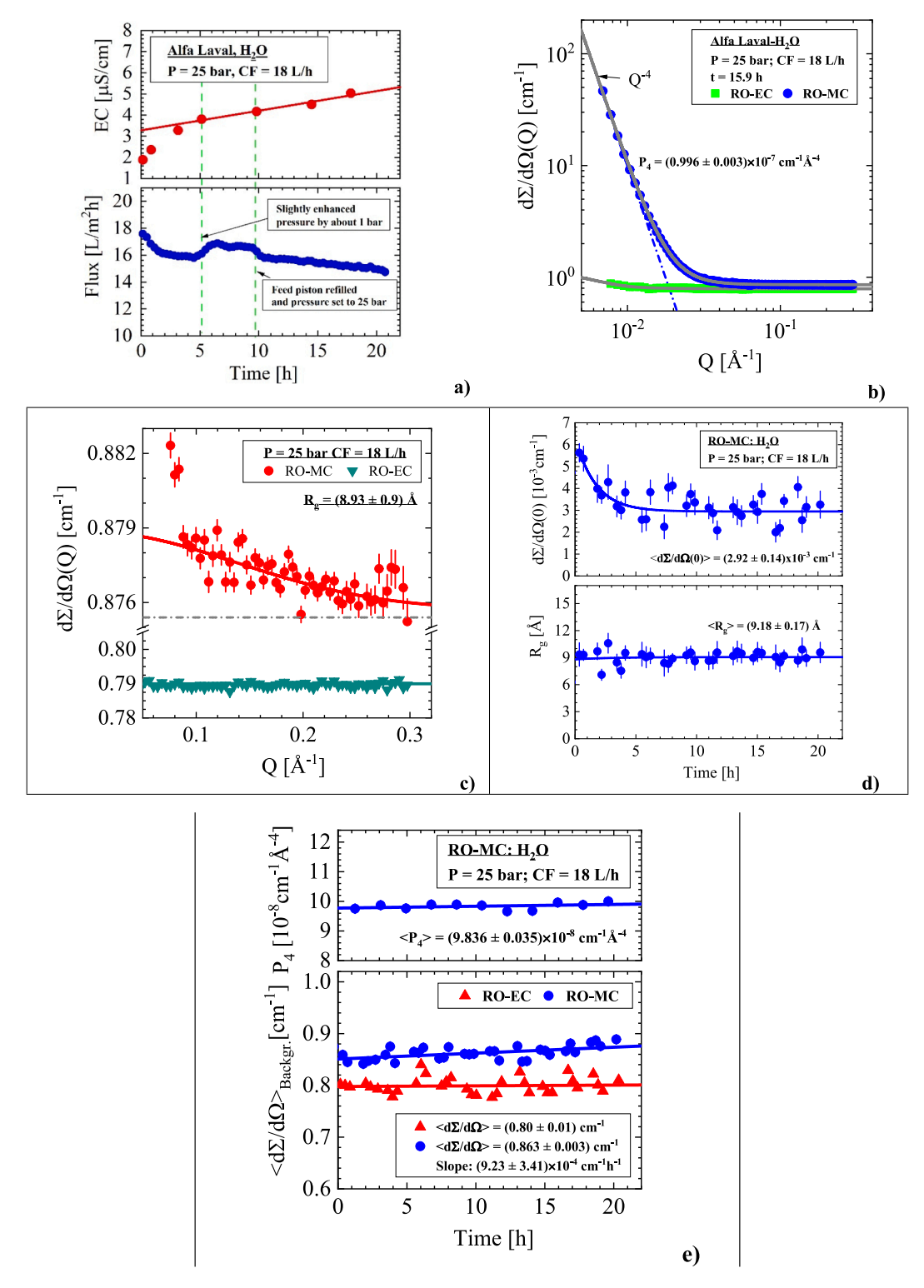


Fig. 9. Parameters of salt-free H₂O experiment. a) Permeate flux and electric conductivity as well as SANS data (b) at small and (c) at large Q. (d) and (e) show the time evolution of various SANS parameters.

74~% of the initial value with a time constant of 10~h. In contrast to the last section, permeate flux and EC might be influenced by releases of molecules from the pristine membrane such as observed in former sections. The SANS data in Fig. 10b-e represent relative stable parameters. The Porod constant P_4 of the macropores in Fig. 10b declines by $\simeq 4~\%,$ whereas the background scattering in Fig. 10c increases between 4 and 5~%. The change of these parameters indicates a weakly reducing D_2O

content during operation and thereby a slightly narrowing of the distance to the matching condition of PSU at 38 % D_2O (P4) and, on the other hand a slightly enhancing incoherent background. Two examples of scattering at start (t = 0) and end (13.5 h) of experiment are shown together with the parameters of the nanopores in Fig. 10d and e. The forward scattering $d\Sigma/d\Omega(0)$ in Fig. 10e, despite of large statistical error bars, shows a trend of small decrease, as realized by the linear fitting

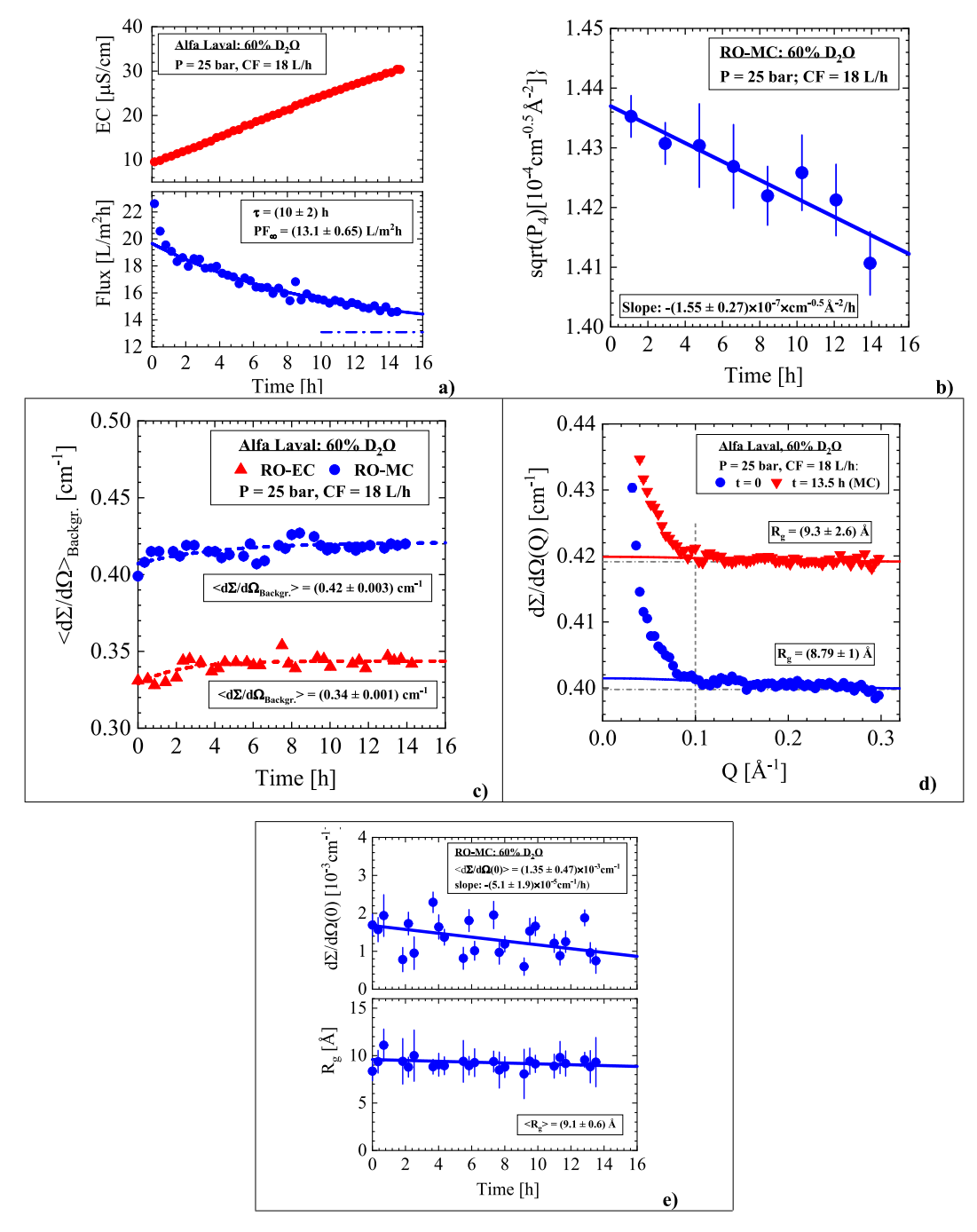


Fig. 10. Experimental parameters of the nominal $60/40~D_2O/H_2O$ feed solution of salt-free water. The Porod constant of the PSU layer in b) as well as $d\Sigma/d\Omega(0)$ in e) are declining, whereas R_g is constant with an averaged radius of $(9.1 \pm 0.6)~\text{Å}$.

routine shown as solid line. This observation is consistent with the decrease of the parameter P_4 in Fig. 10b, which is a measure of the macropore surface area (Eq. (A7)).

3.3. Size of membrane pores determined as function of D_2O concentration of salt-free water at 25 bar and 18 L/h cross-flow

In this section, we compile the SANS parameters of macropores and nanopores and draw our conclusions.

3.3.1. Membrane macropores versus D₂O content

The evaluated parameters from SANS in Fig. 11 change steadily with increasing D_2O content in agreement with the scattering contrast in

Fig. A1b. Fig. 11a shows the pore size (R_g) of the PSU and PP layers as a function of D_2O concentration. The decrease of pore size with D_2O concentration is fitted with a second-order polynomial and shown as a guide for the eye. A similar behavior of R_g is observed for the PP layer at ambient (i.e. 1 bar) conditions in ref. [11], but shows a nearly constant value of $R_g=(0.43\pm0.02)$ mm for the PSU layer with a slight increase for $\rho~<~\rho_{PSU}=2.08\times10^{10}$ cm $^{-2}$ [11] (Fig. 4a). The pressure of 25 bar reduces the PP pore size by about 20 %.

Fig. 11b shows the square root of the Porod parameters of the PP and PSU layers after normalization to the pore size in H_2O $(\Phi_P=0)$ by division with the square of the ratio of $R_g(\Phi_P)/R_g(\Phi_P=0)$. This correction makes sense as the Porod constant is proportional to the pore surface (Eq. (A8)). The normalized Porod data follow straight lines, as normally

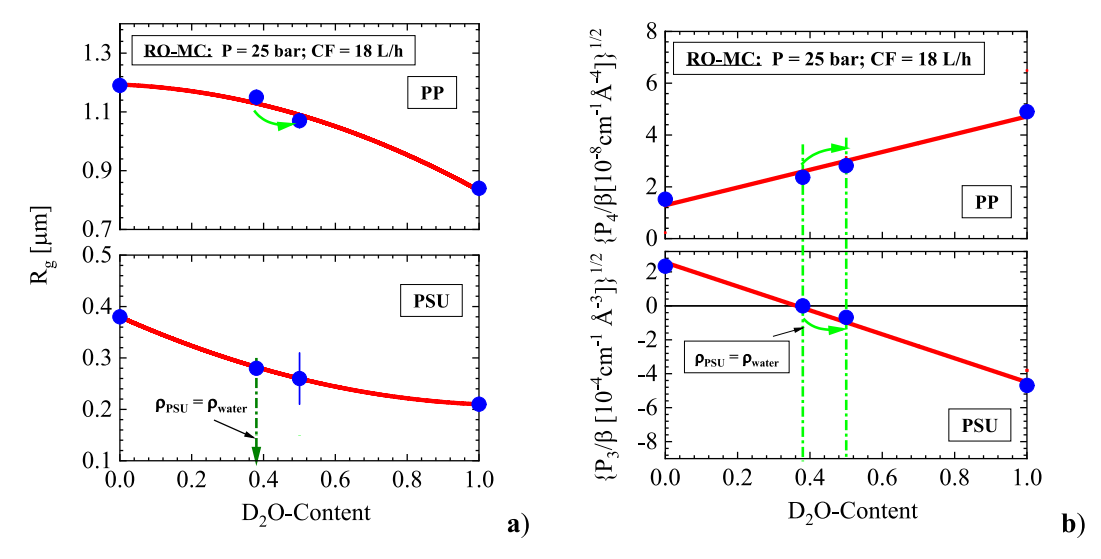


Fig. 11. A) Radius of gyration (R_g) of the PP and PSU membrane layers versus D₂O content. b) Square root of the Porod constants P₄ and P₃ normalized with the square of R_e of H₂O, i.e. $\sqrt{\beta} = R_e (\Phi)/R_e (\Phi = 0)$ following straight lines indicating the decline of pore size as shown for R_e in a).

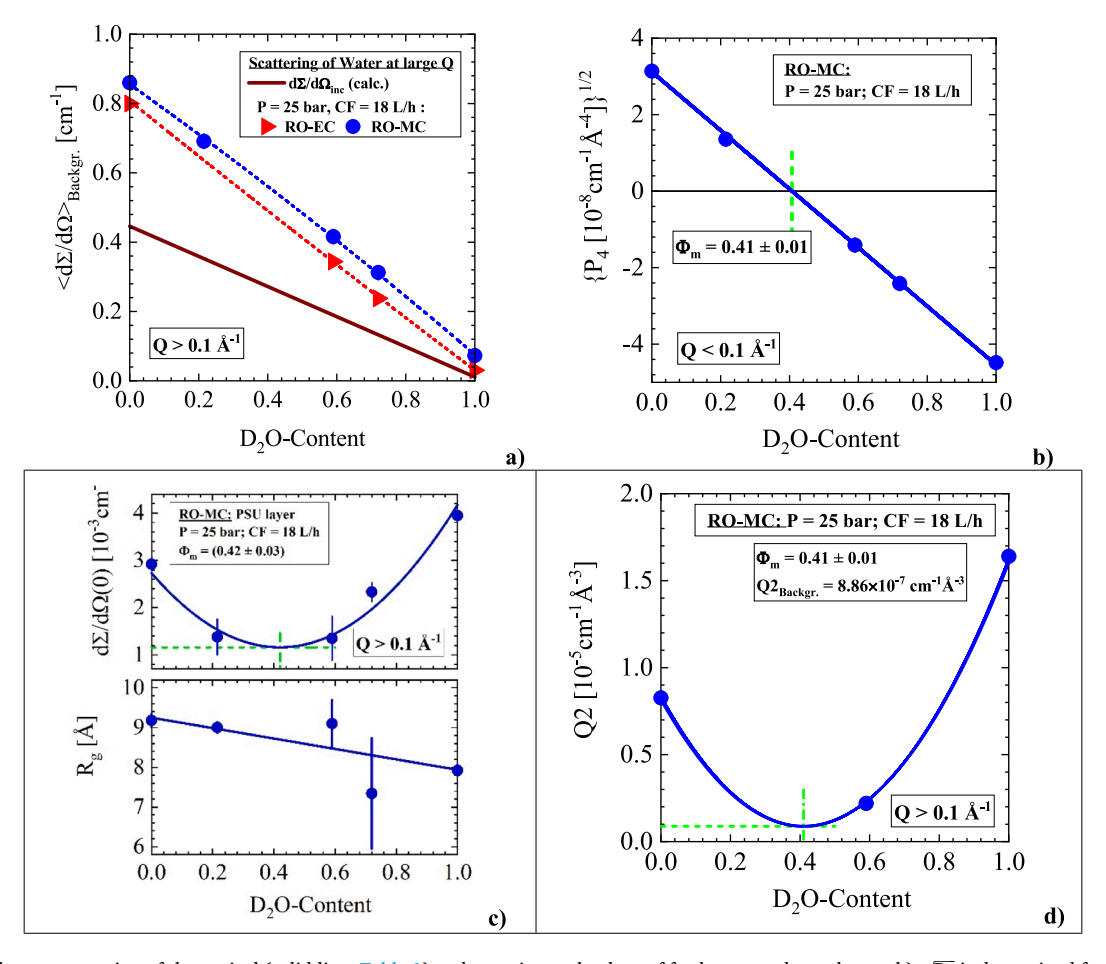


Fig. 12. A) Incoherent scattering of theoretical (solid line; Table 1) and experimental values of feedwater and membrane. b) $\sqrt{P_4}$ is determined from macropores of the PSU layer showing its matching position near the calculated $\Phi_m=0.38~D_2O$ water mixture (Table A2 and Fig. A1b). c) For the same reason, $d\Sigma/d\Omega(0)$ of the nanopores are attributed to the PSU layer ($\Phi_m=(0.42\pm0.03)$). The radius of gyration R_g decreases with D_2O by about 14 %. The large error bars of R_g at 0.6 and 0.7 D_2O content are due to low scattering contrast. The data of $d\Sigma/d\Omega(0)$ shows no matching at Φ_m , i.e. $d\Sigma/d\Omega(0)\neq 0$ indicating partially closed nanopores also explaining the apparent decline of the pore radius. d) Q2 of nanopores shows its minimum at $\Phi_m=(0.41\pm0.01)$ as described by Eq. (1) considering an about 10 % large $\Delta\rho_{PSU}$ and "background" from scattering seemingly of closed pores.

expected from the square root of the scattering contrast $\Delta \rho$, but in this case also from the variation of the pore surface area, which in this way confirms the variation of the pore sizes with D_2O content.

At this point, the 50/50 D₂O/H₂O experiment (section 3.1.3) should be mentioned, which shows a continuous change in the direction of the nominal D2O content for more than 20 h (Fig. 7), as indicated by the green arrows in Fig. 11 for the corresponding variation of Rg and the Porod constants. At the beginning of the experiment, the scattering contrast of the PSU layer is close to the matching value ($\rho_{PSU} = 2.08 \times 10^{-6}$ 10¹⁰ cm⁻², Fig. 7b), that after 2.6 h of treatment shows a D₂O content of 38 %. This value determines the zero crossing of the P3 parameter and must be identical for the corresponding P₄ value. After 20 h of operation, both parameters correspond to a feed solution with the nominal D₂O concentration of about 50 % vol. These data are confirmed by Σ_{SANS} of the RO-EC cell (lower curve in Fig. 6b), which is essentially determined by the incoherent cross-section of the water being 40 times smaller for D_2O than for H_2O (Table 1). The observed 23 % vol decrease of Σ_{SANS} is slightly larger than the 19 % vol resulting from incoherent scattering (Σ_{inc}) , when the D₂O concentration is changed from 38 to 50 % vol.

Fig. 11a shows the radii of the micropores of the PP and PSU layer, which decrease with increasing D₂O content. At first glance, this is a strange result, since the size of membrane pores should not depend on the D₂O content. The explanation of this observation should be preceded by the following statement, namely that the pores measured with SANS are averaged over the entire volume irradiated with neutrons. Decisive for our observation is the presence or absence of closed pores that are not accessible to water. If there were no closed pores, we would get the same number for the pore size for all scattering contrasts (all pores have the same $\Delta \rho$). If the pores have a certain size distribution and closed pores are present, we would get the same number for the pore size only for the dry membrane (all pores have the same $\Delta \rho$), but different values (as we observe) if we expose this membrane to water with different scattering contrasts, i.e. different concentrations of H2O/D2O (closed and open pores have different $\Delta \rho$). This also means, that the SANS contrast variation is sensitive to the degree of open and closed pores.

3.3.2. Membrane nanopores versus D₂O content

The SANS parameters of the nanopores are summarized in Table 1 and parts of them are plotted in Fig. 12. Fig. 12a depicts the incoherent background scattering evaluated from $d\Sigma/d\Omega_{inc}$ of H_2O and D_2O (solid line) [32,33] as well as the corresponding scattering at large Q, as shown, for example, in Fig. 8b of water from the RO-MC (blue) and RO-EC (red) cells following straight lines from $d\Sigma/d\Omega_{inc}$ but are a factor of about two larger because of inelastic incoherent contributions of the water molecules [34,35]. The RO-MC cell shows a few percent larger $d\Sigma/d\Omega_{inc}$ from additional incoherent background scattering of the membrane. The two fitted straight lines also prove the D2O content of the feed solutions and the membrane. Fig. 12b shows the square root of the Porod constant as a function of D₂O content, which, according to Eq. (A8), follows a straight line with zero crossing at $\Phi_{\rm m} = (0.41 \pm 0.01)$, indicating a scattering contrast near the PSU membrane layer of $\Phi_{\rm m}({\rm PSU}) = 0.38$ (Fig. A1b). This shows that the scattering fraction at small Q is essentially determined by the pores of the PSU layer, which is also evident from Fig. 1b and our previous studies in [12].

The parameter $d\Sigma/d\Omega(0)$ in Fig. 12c represents the scattering of nanopores (Table 1) measured at $Q>0.1~\text{Å}^{-1}$, which follows a parabolic function according to Eq. (A4) quite well, with a minimum at $\Phi_m(D_2O)=(0.42\pm0.03)$. This value is slightly larger than the expected PSU value of $\Phi_m(D_2O)=0.38$ but appreciably smaller than the corresponding PA surface layer value of $\Phi_m(D_2O)=0.53$ (Fig. A1b) providing a clear indication of their position in the membrane. The size of the nanopores can be calculated for spherical pores as $R_P=1.29\times R_g$, i.e. about 11.6 Å. This value is confirmed by the ratio of $d\Sigma/d\Omega(0)/Q2=V_P/2\pi^2$ determined for the H_2O fluid delivering $V_P=6.97\times10^3~\text{Å}^3$ or $R_P=11.8~\text{Å}$. A slightly smaller radius of 10.4 Å is obtained for the D_2O

fluid in qualitative agreement with the corresponding R_g numbers in Table 1. The corresponding volume fraction is determined to be $\Phi_P=(2.94\pm0.3)$ % vol and (2.3 ± 0.4) % vol based on $(d\Sigma/d\Omega(0),V_P)$ and Q2, respectively.

Fig. 12d shows the Q2 values of nanopore scattering as a function of D_2O content for the three samples in section 3.2. These Q2 values are quantitatively described by Eq. (1), which is shown

$$Q2 = \{9 \times 10^{-3} \times [0.2 + 2.641 - 6.945 \times \Phi_{D_2O}]^2 \times 10^{-4} + 8.86 \times 10^{-7} \} cm^{-1} \text{ Å}^{-3}$$
 (1)

as a solid line. The square root of the bracket represents the scattering contrast $\Delta\rho^2=[(0.2+\rho_{PSU})-\rho_{water}]^2$ of PSU pores corrected according to $\rho_{PSU}=(0.2+2.08)\times 10^{10}\,cm^{-2}$ in order to account for the slightly larger Φ_m , i.e. $\Phi_m(D_2O)=(0.42\pm0.03)$ instead of the calculated $\Phi_m(D_2O)=0.38$ (Table A2). The last term in Eq. (1) has the meaning of background scattering such as from the closed nanopores also observed for $d\Sigma/d\Omega(0)$ in Fig. 12c. The pre-factor of 9×10^{-3} corresponds to $2\pi^2\,\Phi_{Pore}$ (Eq. (A9) delivering the volume fraction of open nanopores according to $\Phi_{Pore}=4.56\times 10^{-4}$, which normalized to the thickness of the PSU layer accordingly $(0.172\,cm/40\,\mu m)=43$ delivers the average nanopore volume fraction of $\Phi_{Pore}=1.96~\%~vol$.

Nanopores of slightly smaller size, namely R = (8 \pm 0.1) Å and larger volume fraction of (6.2 \pm 0.3) % vol were detected in standalone PA layers [12] (Table A2), indicating that nanopores are part of the active (selective) PA layer as well of the (non-selective) PSU support layer. The pore number density N_P = Φ_P/V_P is determined to be 2.8 \times 10¹⁸ cm⁻³ for the PSU layer and an order of magnitude higher value of 2.9 \times 10¹⁹ cm⁻³ for the PA layers.

4. Summary and discussion

4.1. General comments

We have presented operando SANS studies on reverse osmosis with different salt-free D₂O/H₂O isotope mixtures. The experiments were performed on Alfa Laval RO98pHt membrane samples with a transmembrane pressure of P = 25 bar and a crossflow of 18 L/h. The isotope mixtures were selected to identify the pores in each membrane layer by neutron contrast variation [11]. This is an important point because the scattering pattern is a signal across all layers of the membrane, as illustrated in Fig. 1. Unfortunately, the scattering of the selective polyamide (PA) layer is very low compared to the other two layers due to its relatively small thickness (Table A3). However, we know from earlier SANS experiments on standalone PA layers, that nanopores of radius and volume fraction of respectively (8 \pm 0.1) Å and (6.2 \pm 0.3) % vol are elements of a network morphology with a typical correlation length ξ_S = $(1.42 \pm 0.02 \, \mu m)$ [12] (Fig. 5a), allowing a comprehensive discussion on the pore structure of the entire three layers of the membrane. The nanopores of the PA and PSU layers have approximately the same size, which makes it difficult, if not impossible, to assign the pores. The schematic diagrams in Fig. 13 describe the pore structures of all three layers as determined by our SANS investigations. The radii and structural correlations of the macro- and nanopores determined using SANS are shown for 100 % H₂O scattering contrast representing an overall average over the sample volume. Error bars refer to statistical errors of the respective fits. When comparing with results from other studies systematic errors have to be added.

It is sometimes argued that imaging techniques such as SEM show much larger macropores in RO membranes than SANS and therefore create uncertainty in the data from SANS. We therefore need a discussion on this topic. In particular, we need to consider the strengths and limitations of the usual methods for characterizing the overall pore structure of RO-TFC membranes. A commonly used method for determining pore size in RO polyamide membranes is scanning electron

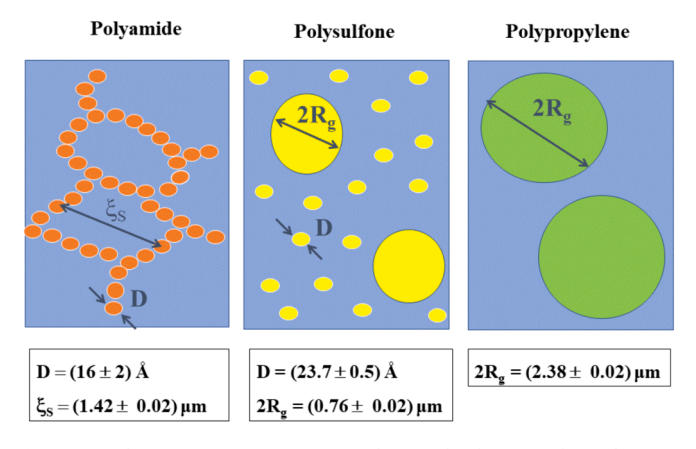
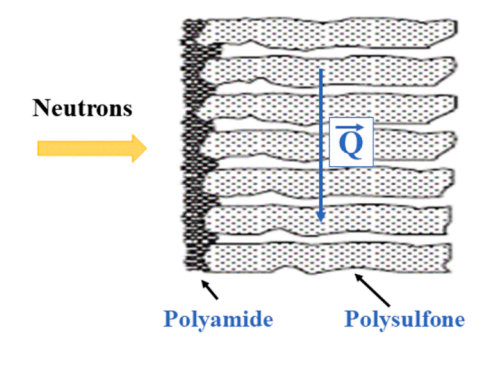


Fig. 13. A schematic representation in analogy to the three membrane layers in Fig. 1a shows the diameters and structural ratios of the pores determined by means of SANS. Nanopores were assumed to be spherical with diameter D, while macropores usually have a more complicated shape [36] and their size is therefore given by the measured gyration radius R_g.

microscopy (SEM). An example of such an image is shown in Fig. 14. A schematic design of the PSU support and PA active layer following Melin et. al. [38] is shown in Fig. 14a, whereas Fig. 14b shows a corresponding SEM micrograph published in [37] (Fig. 2). The SEM micrograph shows a broad size distribution of channel-like pores from about 10 μm in the bulk to 0.5 µm near the interphase to the PA active surface layer. It is important to realize that SANS determines the dimension of pores only in direction of the scattering vector Q orientated perpendicular to the path of the neutrons, i.e. the width of the channels, as explained in context with Eq. (A1). To understand the pore morphology of TFC membranes and how they work, one must deal with pore sizes ranging from less than nm to more than 10 µm. Such a wide range of length scales cannot be analyzed by a single experimental method. This means that the resolution limits of the various experimental techniques need to be examined more closely, as well as their strengths and weaknesses in terms of sample preparation and statistical relevance of the data. This issue was raised by Freger [39] with respect to the "unawareness of fine structure, presumably because of certain resolution gaps". He applied transmission electron microscopy (TEM) in order to explore the "intermediate range between nanoscopic and microscopic". The PSU and PA part of the membrane was cut into 60 to 90 nm thick slices parallel to the membrane surface and stained with uranyl nitrate or sodium tungstate to visualize the pores in the TEM. Pores on the order of $0.2~\mu m$ were observed in the PSU layer of the high-pressure saline water membranes SWC-1 and the high-flux RO membranes ESPA-1 in consistence with our SANS data. The discrepancy with the SEM data in Fig. 14b becomes clear from the pore anisotropy in the PSU layer.



4.2. Macropores of PP and PSU

Pores of μm size are found in the PP membrane layer showing a Q^{-4} power law at large Q indicating a flat surface area (Eq. (A8)). An average R_g of, respectively, (0.84 \pm 0.01) μm and (1.19 \pm 0.01) μm is observed for D_2O and H_2O in Fig. 3b and 5b. Both radii decrease slightly by 3 to 4% during operation. The radius R_g of the 50/50 D_2O/H_2O shows a larger decrease of about 6%, i.e. from 1.15 μm to 1.08 μm , which follows an exponential behavior with a time constant (3.1 h) and which is similar to the compositional change in Fig. 7c. A smaller pore size of about 30% in D_2O and 50/50 D_2O/H_2O fluid in Fig. 7c was also found for the PP layer at ambient conditions from contrast variation with D_2O/H_2O and supercritical CO_2 and CD_4 fluids as function of pressure [11].

The pores of the PSU layer are about three times smaller than the pores of the PP layer (Fig. 3b,c and Fig. 5b.c) and show a fractal surface structure according to the $Q^{\text{-}3}$ power law (Fig. 5a). For $Q>Q_T=5\times 10^{\text{-}3}$ Å $^{-1}$ the $Q^{\text{-}3}$ power law changes to a $Q^{\text{-}4}$ power law (Fig. 9b), i.e. the roughness of the surface layer is limited to length scales greater than about 200 Å ($1/Q_T$), i.e., at greater Q_T the surface of the macropores appears smooth (the index T stands for transition). The size of the pores is $< R_g> = (0.21\pm 0.01)~\mu m$ and $< R_g> = (0.38\pm 0.01)~\mu m$ for D_2O and H_2O , respectively, D_2O again showing a smaller size of 55 %. The PSU layer in $50/50~D_2O/H_2O$ resulted in a pore radius of $< R_g> = (0.25\pm 0.05)~\mu m$ after 13 h of treatment, which is related to the increase in D_2O concentration near the PSU matching condition at smaller times (Fig. 7b).

The "intensity" parameter $d\Sigma/d\Omega(0)$ is constant for D_2O (Fig. 3c) while for the following experiment with H_2O (Fig. 5c and d) an increase by a factor of 1.96 and 2.2 is observed for $d\Sigma/d\Omega(0)$ and P_3 , respectively, at constant pore size (R_g) . This sharp increase in intensity during the experimental period of 7 h without obvious saturation is interpreted as the slow exchange of residual D_2O from the previous experiment in the pores. This process is illustrated in Fig. 5e showing the relative change of the PSU scattering contrast, i.e. $[(\rho_{PSU}-\rho_{Water})/\rho_{PSU}]^2$ as a function of the D_2O content in the PSU macropores. The observed relative increases in $d\Sigma/d\Omega(0)$ and P_3 are shown as red and green arrows, corresponding to an initial D_2O content of about 12% of the water in the PSU pores at the beginning of the experiment. The lack of saturation indicates an even higher D_2O content of the water in the PSU macropores at the beginning of the experiment.

4.3. Nanopores in the PSU support and PA active layer

Nanopores are only observed in the PSU layer as shown in Fig. 12c. The pore size given as the sphere radius R_P was determined from the radius of gyration R_g in Table 1 and Fig. 12c according to $R_P=\sqrt{5/3}\,R_g$ [28] (page 159). The radius for D_2O settles after 10 h at a < $R_P>=$ (10.2

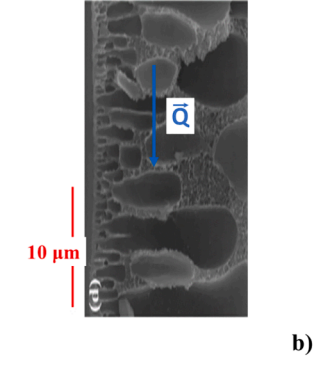


Fig. 14. Schematic design of composite membrane following Melin et. al. [38]. b) SEM micrograph of PSU layer [37] (Fig. 2) showing a broad size distribution from about $10 \mu m$ in the bulk to $0.5 \mu m$ near the interphase to the PA active surface layer. SANS determines the dimension of pores in direction parallel to the scattering vector Q orientated perpendicular to the path of the neutrons. This means that SANS determines the width of the channels.

a)

 \pm 0.2) Å from the slightly larger value of about 13 Å (Fig. 8d). The nearly 30 % decline of the nanopore dimension can be understood from equilibration of a pristine membrane. The same membrane exposed to H_2O (Fig. 9d) shows a constant radius of < $R_P>=$ (11.8 \pm 0.2) Å over the process of 20 h. The 60/40 D_2O/H_2O mixture in (Fig. 10e) shows a constant < $R_P>=$ (11.7 \pm 0.8) Å. These values result in an average total size of < $R_P>=$ (11 \pm 0.8) Å and a volume fraction of $\Phi_P=$ (2.94 \pm 0.3) % vol and (2.3 \pm 0.4) % vol (or 1.96 % vol from Eq. (1)) based on $(d\Sigma/d\Omega(0),V_P)$ and Q2, respectively.

Nanopores in the PA layer play a crucial role in the water transport mechanism through the RO membrane. Whether the transport process is described by the solution-diffusion model or by permanent pore flow is still controversial. Since the PA active layer is often considered nonporous, the solution-diffusion model has long been considered the basis for water transport through the membrane. Baker [2] (chapter 2) gives an estimate of critical size between 0.5 and 1 nm diameter between "truly solution-diffusion and truly nanoporous membranes". Fig. 13a shows for the polyamide pores a diameter of 1.6 nm being part of a percolation network of $\xi = 1.4 \,\mu m$ size [12]. Positron annihilation lifetime spectroscopy (PALS) of the same study determined a diameter of about 0.6 nm for the channels of a percolation network thereby enabling the stated 99 % of salt rejection. Contrast variation with supercritical CO₂ proved that the pores of the PA active layer are accessible to liquids and therefore must be connected to each other [12] (Fig. 4). Molecular simulations by Ridgway et al. in ref. [40] (Fig. 7) confirmed this scenario depicting the nanopores and channels for the transport of the water molecules.

From our data of the PA [12] and PSU layers, we obtain an indication of the preference of the pore-flux transport mechanism model. Such transport mechanism is also proposed in recent literature. In our opinion, convincing data on this subject have been recently presented based on quasi-elastic neutron spectroscopy, in which the mobility of $\rm H_2O$ and of the PA host molecules was determined by quasi-elastic incoherent scattering of the hydrogen of water and PA molecules [34,41,42]. By hydrating the membrane with $\rm H_2O$ and $\rm D_2O$, the mobility of water and polymer molecules could be distinguished. A long-range and a localized diffusion mode were observed for the water and PA molecules, respectively.

The discussion on the pore structure of active PA layers based on TEM tomography shows different scenarios and thus once again underlines the complementarity of imaging and scattering methods. Pacheco et al [43] (Fig. 7) presents a 3D visualization of the polyamide internal nanostructure, confirming the existence of numerous voids between 0.015 μm and 0.1 μm , interpreted as the structural feature explaining the difference in water permeability of the different membranes. Similar conclusions are made by Lin et al [44] finding voids of "tens of nanometer in diameter" and volume fraction between 15 – 32 % not forming "passageways", which, however, fill with water and whose presence can increase water permeability by a factor of up to 5.

Another electron tomography study was conducted by Culp et al. [45] performed on membranes compressed in a cross-flow system at 150 PSI (10.2 bar) for 12 h to simulate the operating conditions of a RO system and represent a more realistic membrane structure. They found closed void fractions of 0.12 % and 0.04 % for the SWHR-C and BWXLE-C membranes, respectively, more than two orders of magnitude lower than previously reported. Pores of size between 1 and 5 nm were not detectable in a layer with high polymer density (low porosity) due to the lack of resolution of the experimental method. A recently published study using low-dose electron tomography and quantitative morphometry on PA membranes for waste water reclamation was conducted by Song et al. [46]. The 3D reconstruction shows PA crumples formed from PA layers of 15–20 nm thickness thereby increasing the active surface layer of the membrane.

All of these local microscopic methods require special sample

preparation and sometimes show a PA layer with high polymer density and a layer thickness of the order of 10 nm of highly crumpled shape [47,48]. The size of the area of the crumpled PA layer influences the membrane permeability and is therefore a relevant parameter. SANS and PALS provide a detailed insight into the "high-PA polymer" layer as described by Pipich et al. in [12] and is shown schematically in Fig. 13a. As already mentioned, it determines the transport mechanism of the water molecules in the active PA layer [2]. In this regard, the examples presented demonstrate that SANS and the local methods such as SEM and TEM are necessary for a complete picture of the microscopic morphology of TFC membranes.

4.4. Permeate flux and electric conductivity

The permeate flux was determined by weighing the permeated water with a balance, while the electrical conductivity (EC) was measured in the closed circuit of the feed water [14]. We always observe an exponentially decreasing permeate flux over time up to 40 h with a time constant τ between 5 and 17 h together with a continuous increase of the EC value, although we always started with salt-free water (Fig. 8a). The observed decline of permeate flux seems to have several reasons. One reason can certainly be seen in the electrical conductivity, namely, that the originally salt-free water in our device is constantly contaminated with charged and uncharged components leached from the membrane. This is particularly evident in the D₂O experiment of Fig. 2 from the comparison of the EC and total macroscopic scattering cross-section Σ_{SANS} (Fig. 2). The slope of EC in Fig. 2a changes after 6.95 h from (2.65 ± 0.01) mS/(cm h) to (1.49 ± 0.01) mS/(cm h) by nearly 50 %, which coincides with the shape of Σ_{SANS} separating the exponentially increase and decrease at 6.5 h with stabilization after about 15 h. The relaxational time constant τ of permeate flux of (17 \pm 6) h is seemingly correlated with the time of stabilization of Σ_{SANS} after 15 h. A similar behavior is observed for the Porod constant P₃ of the PSU layer (Fig. 3c), indicating the role of the PSU layer on the permeate flux.

The time constants from the other experiments, e.g., for the $\rm H_2O$ liquid, are much shorter: (4.8 \pm 1.5) h for the permeate flux (EC) and the corresponding (5.3 \pm 1.1) h for Σ_{SANS} , which are accompanied by a linear increase of electrical conductivity (Fig. 4), showing a possible correlation between dissolved ion content (EC and SANS) and permeate flux. Another example is shown for the 50/50 $\rm D_2O/H_2O$ fluid in section 3.1.3, showing a change of $\rm D_2O$ concentration from 0.36 to 0.50 (Fig. 7). The permeate flux decreases exponentially with $\tau=(5.6~\pm~0.5)~h$ (Fig. 6) whereas Σ_{SANS} increases exponentially with $\tau=(4.1~\pm~0.8)~h$ (Fig. 6) supported by changes of $\rm d\Sigma/d\Omega(0)$ (PSU, Fig. 7b) with $\tau\simeq 5~h, P_4$ (PP, Fig. 7c) with $\tau=(5.4~\pm~0.4)~h,$ and Q2 (PP, Fig. 7d) with $\tau=(4.4~\pm~0.3)~h$. These matching constants of time could indicate an influence of $\rm D_2O$ concentration on permeate flux.

This is possibly the first time that a comparison of permeate flux, electrical conductivity and pore structure evolution has been made using SANS data. The correlations shown are complex and could have several reasons, such as the removal of some preservatives added by the manufacturer, such as glycerine. On the other hand, our SANS studies with salt solutions (SSE [47]) show an EC between 3 and 4 mS/cm, i.e. two to three orders of magnitude higher conductivity. From this, one could conclude that conductivities in the μ S/cm range are not at all relevant for the RO process itself. Rather they indicate the high sensitivity of the SANS signal to any change in the feed. The aim of further systematic investigations will be to find clear correlations between permeate flow and ion concentration (concentration polarization) of the feed as well as the pore structure of the membrane and the scaling of the PA membrane surface.

5. Conclusions

In this article, operando investigations are carried out using smallangle neutron scattering (SANS) on a reverse osmosis (RO) membrane with salt-free water at 25 bar and 18 L/h crossflow for approx. 20 h (in one case even 40 h). Contrast variation of neutron scattering with D_2O/H_2O mixtures was performed using two SANS devices with different Q ranges to cover pore sizes from 2 nm to μm . A detailed analysis of the evolution of the pore structures of both membrane support layers PP and PSU was carried out, whose main results are summarized schematically in Fig. 13. The detailed conclusions are:

- Contrast variation identified the pores of the PP and PSU membrane layer, but also showed partially closed pores by their smaller average size at larger D₂O concentration (Fig. 11a, 12 and 12c).
- Nanopores are only observed in the PSU layer, as shown in Fig. 13. The average pore diameter of the nanopores is about 24 Å and their volume fraction is about 2 % vol (Fig. 12c and Eq. (1)).
- During reverse osmosis operation, the size of the macropores decreased slightly by a few percent (Fig. 3a), while the size of the nanopores in the PSU layer of an untreated membrane decreased by about 30 % and stabilized to an equilibrium value after about 15 h of treatment (Fig. 8d).
- The exchange of D₂O to H₂O in the macropores of the PSU layer could be followed experimentally and lasted more than 7 h (Fig. 5).
- It is shown that SANS and local methods such as SEM and TEM are complementary methods and can only provide a complete picture of the pore structures when used together. This is particularly evident in the detection of nanopores in the PSU layer (Fig. 14).
- The total macroscopic scattering cross-section Σ_{SANS}, measured with the VSANS device, shows qualitatively the same behavior as the EC (e.g. Fig. 2).
- Even after pretreatment of the membrane prior to the SANS experiments, there was a slight increase in contamination of the water in the feed circuit, as measured by a slight increase in total SANS scattering as well as in electrical conductivity in the μ S/cm range. However, the latter is two to three orders of magnitude lower than the electrical conductivity of the salt solution (SSE) we use and is therefore of lesser importance.
- Further contamination of the salt-free water was detected by a very low concentration of PP particles of $\Phi_{PP} \simeq 2.06 \times 10^{-3}$ % vol and R_g

= (1.48 ± 0.12) µm radius of gyration in the RO-EC cell (membrane free) by contrast variations, as described in detail in Appendix A4.

Funding

This work was funded by the German–Israeli Foundation for Scientific Research and Development (GIF), grant No: I-101–307.4–2013.

CRediT authorship contribution statement

Vitaliy Pipich: Writing – review & editing, Validation, Investigation, Formal analysis, Data curation. Thomas Starc: Methodology, Investigation. Roni Kasher: Writing – review & editing, Validation. Winfried Petry: Writing – review & editing, Visualization, Validation, Formal analysis, Conceptualization. Yoram Oren: Writing – review & editing, Supervision, Methodology, Investigation, Conceptualization. Dietmar Schwahn: Writing – review & editing, Writing – original draft, Project administration, Methodology, Investigation, Formal analysis, Data curation, Conceptualization.

Declaration of competing interest

The authors declare that they have no known competing financial interests or personal relationships that could have appeared to influence the work reported in this paper.

Data availability

Data will be made available on request.

Acknowledgments

SANS experiments were performed at, respectively, the KWS3 and KWS1 at the Heinz Maier-Leibnitz Zentrum (MLZ), Garching, Germany. D.S. would like to thank Prof. Dr. Stephan Förster, head of the Jülich Centre for Neutron Science (JCNS-1) and Institute for Complex systems (ICS-1) at the Forschungszentrum Jülich GmbH for his hospitality.

Appendix A

The Appendix provides the relevant scattering laws of this manuscript as well as characteristic parameters of the RO membrane and the desalination SANS cells RO-MC and RO-EC we need for the analysis and interpretation of the scattering data. It also shows the observation and identification of extremely low concentration of micrometer large polypropylene impurities in the salt-free water of the feed loop using SANS contrast variation.

Appendix A1. Calibration of SANS scattering intensity in absolute units

The intensity of scattered neutrons in absolute units is expressed as the differential macroscopic cross-section $d\Sigma/d\Omega(Q)$ in units of cm⁻¹ (i.e. scattering per cm³ of sample volume) as a function of the magnitude of the scattering vector Q determined according to Eq. (A1) from

$$|Q| = (4\pi/\lambda)\sin(\delta/2) \tag{A1}$$

the scattering angle δ and the wavelength λ of the neutrons (in the present case: $\lambda=7$ Å at KWS1 and 12.8 Å at KWS3). The scattering vector \underline{Q} is proportional to the momentum transfer of the neutron according to $\hbar \underline{Q}$ (\hbar Planck's constant h over 2π) and determines the projection of the structural distances in the direction of \underline{Q} according to the amplitude of the form-factor $A(\underline{Q})=\int d_3\underline{r}\,\rho(\underline{r})\exp(-i\,\underline{Q}\,\underline{r})$ [28] (p. 160). Objects of radius R are basically explored in a Q regime of the order of 1/R, i.e. $Q\sim 1/R$. In a first step, the macroscopic cross-section $d\Sigma/d\Omega(\underline{Q})\propto |A(\underline{Q})|^2$ is determined from the experimental scattered neutron intensity $\Delta I_D(\underline{Q})$, which according to Eq. (A2) is proportional to the incident intensity I_0 , the sample thickness D_S , the

$$\Delta I_D(\underline{Q}) = I_0 D_S T \frac{d\Sigma}{d\Omega} (\underline{Q}) \Delta \Omega_D \tag{A2}$$

sample, transmission coefficient $T = I_0^* / I_0$, and the space angle element $\Delta\Omega_D$ of the detector. The transmission coefficient describes the attenuation of the primary (i.e. non-scattered out of the primary beam) neutron intensity (I_0^*) after having passed the sample. The calibration of $d\Sigma/d\Omega(Q)$ in absolute units (usually in cm⁻¹) is performed by an additional measurement of a sample of known $d\Sigma/d\Omega(Q)$ or by a direct beam $I_0^* = T \times I_0$

determination in both cases with the same collimator setting [48,49].

The thickness of the sample is a relevant parameter for reliable absolute calibration. Usually, homogeneous solids or liquid fluids in cells have a fixed thickness. However, both SANS cells for reverse osmoses (RO) desalination show a more complex behavior with respect to their thickness as both cells (RO-MC and RO-EC)) are usually exposed to different pressure fields and cross-flow velocities through the feed solution thereby leading to changes in thicknesses of the channel height, i.e. the volume of the feed the neutrons have to pass. The increase of pressure from ambient to 25 bar increases the channel height by 26 % from 0.137 to 0.172 cm as determined from neutron transmission in combination with measurement of the external dimensions. As we performed

Table A1 Dimensions (D_S in Eq. (A2)) of empty (RO-EC) and membrane cell (RO-MC) with the RO membrane RO98pHt from Alfa Laval. We assume that a change in membrane thickness with pressure is negligible compared to changes in cell dimensions.

Position/ Pressure	Total channel height [cm]	RO98pHt [μm]	Permeate spacer [μm]	Channel height of feed [cm]	Cross-section of channel [cm ²]
1 bar					
RO-EC	0.137			0.137	0.62
RO-MC	0.137	300	215	0.086	0.45
25 bar					
RO-EC	0.172			0.172	0.77
RO-MC	0.172			0.121	0.54

the present experiments at constant 25 bar we normalized the SANS data of the cell without membrane (RO-EC) according to its thickness of $D_S = 0.172$ cm, while the scattering of the membrane (RO-MC cell) at the KWS3 diffractometer for Q between 10^{-4} and 2×10^{-3} Å $^{-1}$, was normalized to the thickness of the membrane, i.e. 300 μ m, as the scattering of the membrane is outweighed by orders of magnitude.

Table A1 compiles membrane and permeate spacer thickness as well as height and cross-section of the channel at ambient and 25 bar for the membrane cell (RO-MC) with the Alfa Laval RO membrane and empty cell (RO-EC). The permeate spacer is a plastic mesh directly behind the membrane through which the permeate (potable water) flows out of the RO module [50] (p. 36). The cross-flow of 18 L/h corresponds to an average velocity of 0.10 m/s for a channel cross-section of 0.50 cm². The width of the channel is 4.5 cm. The knowledge of channel height and membrane thickness is important for a trustworthy evaluated $d\Sigma/d\Omega(Q)$ and thereby a precondition for reliable quantitative analysis and interpretation.

Appendix A. 2. SANS scattering laws

Scattering techniques using neutrons and photons as probe are well established tools both from theoretical and experimental aspects. Scattering occurs at domains which differ from their surroundings with respect to chemical composition and/or mass density. Examples of those domains are precipitates and cavities in solid matrices or colloids in solution. This means that SANS is a quantitative method determining structural parameters averaged over macroscopic large volumes of the order of 0.1 cm³. In this respect it is complementary to TEM in which individual domains are made visible.

The differences in chemical composition and/or mass density are expressed by the scattering contrast. The scattering contrast of neutrons is determined by the square of the difference of the coherent scattering length density of the domain (P) and its surrounding (S), namely $\Delta \rho^2 = (\rho_P - \rho_S)^2$. The scattering length density is defined as the sum of the coherent scattering length of the atoms, b_i , of a molecule divided by its volume Ω_M , that is $\rho = \sum_i b_i/\Omega_M$ [33].

In this manuscript, SANS is referred to scattering that mainly emerges from individual domains neglecting possible coherence effects of the domains due to their interaction or excluded volume interaction. The corresponding macroscopic scattering cross-section is determined in Eq. (A3) as product of the form factor F(Q) (F(Q) = 1), the structure factor F(Q) (F(Q) = 1), and

$$d\Sigma/d\Omega(Q) = d\Sigma/d\Omega(0) \times F(Q) \times S(Q) \tag{A3}$$

the scattering cross-section at Q = 0 determined in Eq. (A4) from the volume of the domain (V_P) ,

$$d\Sigma/d\Omega(0) = \Phi_P V_P [\rho_P - \rho_S]^2 \tag{A4}$$

its volume fraction (Φ_P) of the scattering particle, as well as from the scattering contrast $\Delta \rho^2 = [\rho_P - \rho_S]^2$ of the scattering centers discussed below in more detail. We only give the form factor of a spherical object in Eq. (A5) with the radius R [28] (p. 160). We usually analyzed

$$F_{sph}(Q) = \frac{9\left[\sin(QR) - QR\cos(QR)\right]^{2}}{(QR)^{6}}$$
(A5)

 $d\Sigma/d\Omega(Q)$ with the Beaucage equation of Eq. (A6) describing non-specific scattering patterns

$$d\Sigma/d\Omega(Q) = d\Sigma/d\Omega(0)\exp(-u^2/3) + P_a \left[\left(erf\left(u/\sqrt{6} \right) \right)^3/Q \right]^a$$
(A6)

over a large Q range [51]. At $Q < 1/R_g$, $d\Sigma/d\Omega(Q)$ is determined by the first term and corresponds to Guinier's approximation (Eq. (A7)) whereas at $Q > 1/R_g$ by a power law with the exponent α .

$$d\Sigma/d\Omega(Q) = d\Sigma/d\Omega(0) \exp\left[-R_g^2 Q^2/3\right] \tag{A7}$$

The power index $\alpha = 4$ represents the well-known Porod law with the corresponding amplitude factor according to Eq. (A8) with N_P and S_P the number density and surface area of the scattering

$$P_4 = 2\pi N_P S_P \left[\rho_P - \rho_S \right]^2 \tag{A8}$$

particles [28] (p 178). The parameters of Eq. (A6) are: $u=R_g Q$ the product of Q and radius of gyration R_g as well as the scattering $d\Sigma/d\Omega(0)$ at Q=0. An important parameter is determined from the integral $\frac{1}{4\pi}\int d\Sigma/d\Omega(\underline{Q})\ d_3\underline{Q}$ over the reciprocal space representing the "invariant" Q2. This parameter is termed "invariant" as it is independent from domain size and only proportional to the domain volume fractions Φ_P and $(1-\Phi_P)$ ($\simeq 1$ in dilute solutions) and their scattering contrast as shown in Eq. (A9) [28] (p. 28). The total macroscopic scattering cross-sections Σ_{SANS}

$$Q2 = 2\pi^2 \Phi_P (1 - \Phi_P) [\rho_P - \rho_S]^2$$
(A9)

is obtained from integration over the space angle Ω according to $\Sigma_{SANS} = \int_{4\pi d\Omega} \frac{d\Sigma}{\Omega}(Q) \, d\Omega = \frac{1}{k_0^2} \int_0^\infty \frac{d\Sigma}{d\Omega}(Q) \, d_2Q = \frac{2\pi}{k_0^2} \int_0^\infty Q \, \frac{d\Sigma}{d\Omega}(Q) \, dQ$, which for isotropic scattering delivers the expression in Eq. (A10) with the correlation length l_C discussed by Porod in [28] (p 29). However, Σ_{SANS} gives as an integral parameter (Eq. (A10)) information about the pore structure of the total membrane.

$$\int_0^\infty Q \, \frac{d\Sigma}{d\Omega}(Q) \, dQ = \Phi_P(1 - \Phi_P) l_C \left[\rho_P - \rho_S \right]^2 \tag{10}$$

Appendix A. 3. Parameters of the RO98pHt membrane

Knowledge of the scattering contrast $\Delta \rho^2 = (\rho_P - \rho_S)^2$ of the TFC membrane layers in salt-free water (D₂O/H₂O) is important for membrane characterization and has been extensively studied for the skin layer in [12] and for the two support layers in [11] and serves as a reference for the present article. Table A2 compiles scattering length densities (ρ) calculated for the three polymers layers.

Table A2 Relevant parameters of the Alfa Laval RO98pHt membrane. The membrane belongs to the class of thin film composite (TFC) RO membranes made from layers of polyamide (PA), polysulfone (PSU), and polypropylene (PP) with an overall thickness of 300 μm (Fig. 1a). The scattering length density of water follows: $ρ_W = [-0.5608 + 6.945 \times Φ_{D_2O}] \times 10^{10} cm^{-2}$.

Composition	Chemical Formula	Molar Mass [g/mol]	Mass Density [g/mL]	Scattering Length Density $ ho [10^{10}~{ m cm}^{-2}]$
Aromatic Polyamide (PA)	$N_2C_{14}H_{10}O_2$	238	1.44	3.10
Polysulfone (PSU)	$C_{27}H_{22}O_4S$	442.5	1.24	2.08
Polypropylene (PP)	C_3H_6	42.1	0.91	-0.325
Water	H_2O	18.0153	1	-0.5608
	D_2O	20.0286	1.107	6.384

of the TFC reverse osmosis membrane RO98pHt. Table A3 compiles their scattering contrast $\Delta \rho^2$, i.e. their scattering contrast with respect to the aqueous isotope solutions of the feed with different D_2O composition. For better comparison, the scattering contribution of the individual membrane layers is also given as the product of $\Delta \rho^2$ and thickness (D_s) of the corresponding layer; the sample thickness Ds is proportional to the intensity of the scattered neutrons (Eq. (A2)). This number seems helpful, as the thickness of the individual membrane foils is very different. Both, $\Delta \rho^2$ and $D_S \times \Delta \rho^2$ of the three membrane layers in Table A3 are also depicted in Fig. A1b against the D_2O .

Table A3 Scattering contrast $\Delta \rho^2 = (\rho_P - \rho_W)^2$ of the membrane layers exposed to the water isotope mixtures D_2O/H_2O . The brackets give the product of $\Delta \rho^2$ and thickness (D_s) of the corresponding membrane layer for better comparison of the scattered neutron intensity (Eq. (A2)). The average macropore radii of the PSU and PP layers are compiled in the bottom line. The micropore radii of the PSU layer are compiled in Table 1.

Concentration D ₂ O	$\Delta ho^2~[10^{20}~{ m cm}^{-4}]~({ m D_S} imes\Delta ho^2[10^{20}~{ m cm}^{-3}])$				
	Polyamide (PA)	Polysulfone (PSU)	Polypropylene (PP)		
0.00	13.40 (2.68 × 10 ⁻⁴)	6.97 (3.49 × 10 ⁻²)	$5.57 \times 10^{-2} (1.39 \times 10^{-3})$		
0.30	$2.48 (4.96 \times 10^{-5})$	$0.309~(1.55\times10^{-3})$	$3.42~(8.55\times10^{-2})$		
0.50	$0.034~(6.80\times10^{-7})$	$0.697 (3.49 \times 10^{-3})$	$10.50~(2.63\times10^{-1})$		
0.70	$1.70 \ (3.40 \times 10^{-5})$	$4.95 (2.48 \times 10^{-2})$	$21.40~(5.35\times10^{-1})$		
1.00	$10.80 \ (2.16 \times 10^{-4})$	$18.58 \ (9.29 \times 10^{-2})$	45.10 (1.128)		
Thickness D _S [mm]	$\simeq~0.2$	$\simeq 40$	$\simeq 260$		

content showing zero scattering contrast for the PSU layer in a water mixture of 38 % vol D_2O content, whereas nearly zero contrast for the PP nonwoven layer in H_2O (zero scattering for 3.3 % vol D_2O content). The lower part of the Fig. A1b shows that the PSU and PP layers dominate the scattering for all aqueous solutions of the D_2O/H_2O mixture. The degree of scattering of the PA skin layer is too small (orders of magnitude smaller than the PSU and PP layers) to contribute a measurable signal because of its significantly smaller thickness of $\simeq 0.2$ mm.

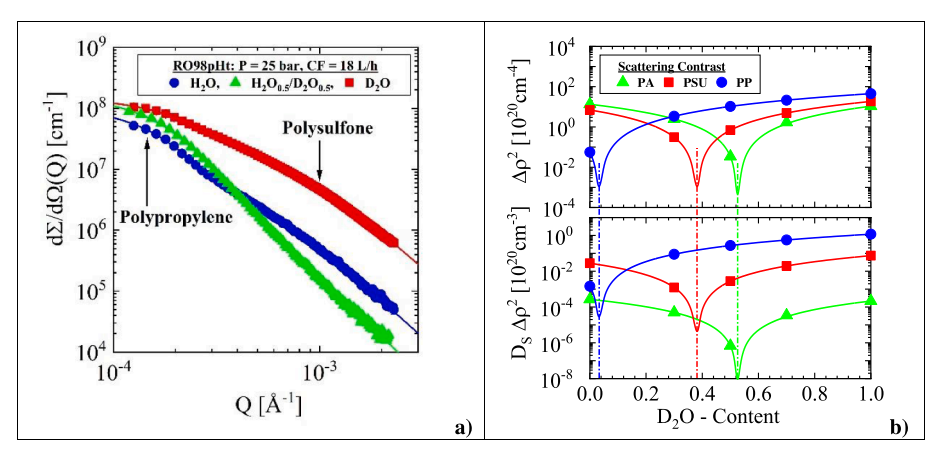


Fig. A1. (a) Scattering patterns of the RO98pHt membrane exposed to different solvents, H_2O (Fig. 5a), D_2O (Fig. 3a)), and the 50 % mixture of H_2O/D_2O (Fig. 7a)), fitted with Eq. shown as solid lines. (b) (top) Scattering contrast of the three membrane layers PA, PSU and PP, and (bottom) the scattering power considering the thickness (D_S) of the three layers exposed. At small / large Q area scattering is dominated by the PP / PSU layer. Scattering from the PP layer continuously increases with D_2O content in consistence with $D_S\Delta\rho^2$ in the lower Figure (b), whereas the PSU layer first declines with D_2O content because of the matching at 40 % D_2O content before increasing again.

Appendix A4. Micrometer-sized impurities in the salt-free water of the feed circuit

We present here SANS data of salt-free $\rm H_2O$, $\rm D_2O$ and a mixture of $\rm D_2O/H_2O$ measured in the RO-EC cell, i.e. the pressure cell without membrane. The water circulates in a piping circuit in which the two pressure cells (RO-EC and RO-MC) are integrated. The experimental conditions are controlled by a piston and a pump that supplies fresh water under pressure and cross flow [13] (Figs. A2 and A3). The volume of the feed circuit is 330 mL. The SANS data, averaged over an experimental period of 10 to nearly 20 h, are shown in Figs A2a-c. Surprisingly, for $\rm D_2O$ in particular, we observe a pronounced scattering instead of the much weaker flat incoherent scattering expected for water, i.e. $d\rm D/d\Omega_{inc}=0.446~cm^{-1}$ and $1.106\times10^{-2}~cm^{-1}$ for $\rm H_2O$ and $\rm D_2O$, respectively – see Fig. 12a, Table 1 of this paper as well as detailed discussion on incoherent scattering in [32]. Figs. A2a and b show the scattering of $\rm H_2O$, the 38/62 $\rm D_2O/H_2O$ mixture, and the $\rm D_2O$ feed solutions. We observe weak scattering for $\rm H_2O$ and a significantly enhanced scattering for the two higher $\rm D_2O$ contents of more than one to two orders of magnitude. Eq. (A6).

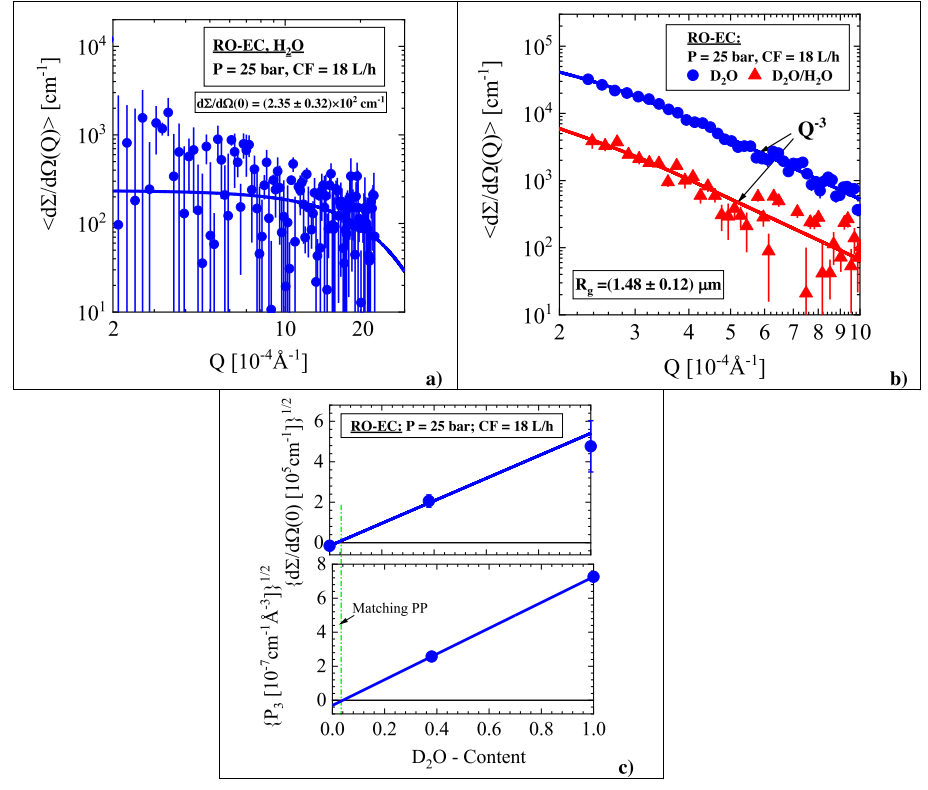


Fig. A2. Time average $<\!d\Sigma/d\Omega(Q)>$ from salt-free water measured in the membrane free cell (RO-EC) with: a) H_2O and b) $\Phi/(1-\Phi)$ D_2O/H_2O by 38/62 as well as D_2O . Scattering delivers nearly zero scattering in H_2O whereas scattering becomes rather strong at larger D_2O content showing a mass fractal dimension. c) The square root of $d\Sigma/d\Omega(0)$ and P_3 of the D_2O volume fractions indicate polypropylene polymer aggregates of 1.48 μ m radius of gyration.

was fitted to these data with the fit parameters R_g and the Porod constant P_3 . The parameter P_3 is the amplitude of the exponential decay at large Q (Eq. (A6)) showing with its exponent $\alpha_S = 3$, i.e. Q^{-3} a fractal dimension indicating a rough surface structure (S) of three-dimensional objects following

a size dependence of the radius R according to $S(R) = S_0 R^{(2-\alpha_S)}$ [28] (p. 190). The SANS data could only be evaluated for $Q > Q_m$ (=2.3 × 10⁻⁴ Å⁻¹) as the scattering below Q_m was still influenced by neutrons of the primary beam. The SANS parameters from the fit are compiled in Table A4 and the square root of $d\Sigma/d\Omega(0)$ and P_3 are depicted in Fig. A2c. These data follow a straight line in consistence with their proportionality to the difference of the coherent scattering length density $\Delta \rho = (\rho_P - \rho_S)$ of particle (ρ_P) and solvent (ρ_S) . Both parameters, i.e. $\sqrt{d\Sigma/d\Omega(0)}$ and $\sqrt{P_3}$ cross zero at the matching position of polypropylene (PP), i.e. at $\Phi(D_2O) = 0.034$. This is a clear indication that individual macroscopic PP particles are dissolved in the original salt-free water of the feed circle. The nominal volume fraction of the D_2O/H_2O isotope mixtures is 50 % vol. However, we found from the corresponding SANS data of the membrane in the RO-MC cell a smaller D_2O concentration of $\Phi_{D_2O} = 0.38$, i.e. 38/62 D_2O/H_2O as depicted in Fig. 7b and Fig. 11.

Table A4Parameters of the "salt-free" water in the feed circle of Fig. A2.

DI-Water (D ₂ O)	$d\Sigma/d\Omega(0)[cm^{-1}]$	R _g [μm]	$P_3 [cm^{-1} \mathring{A}^{-3}]$	$Q_2 [cm^{-1} \mathring{A}^{-3}]$	$V_P[10^{12}\mathring{\text{A}}^3]$
0	$(2.35 \pm 0.32) \times 10^2$		-		_
0.38	$(4.24 \pm 1.26) \times 10^4$	1.48	$(6.61 \pm 0.21) \times 10^{-8}$	2.41×10^{-7}	3.47
1	$(2.27\pm 1.21)\times 10^{5}$	1.48 ± 0.12	$(5.27 \pm 0.11) \times 10^{-7}$	1.83×10^{-6}	2.45

Further analysis delivers Q2 values (Eq. (A9)) of $\simeq 1.83 \times 10^{-6} \text{cm}^{-1} \text{Å}^{-3}$ and $\simeq 0.241 \times 10^{-6} \text{cm}^{-1} \text{Å}^{-3}$ for D₂O and the 38/62 D₂O/H₂O mixture, respectively. The ratio of $d\Sigma/d\Omega(0)$ and Q2 (Eqs. (A(4) and A(9)) delivers an average volume and radius of the PP particles of $\langle V_{PP} \rangle = (3 \pm 0.5) \times 10^{12} \, \text{Å}^3$ and $\langle R_{PP} \rangle = (8.94 \pm 0.54) \times 10^3 \, \text{Å}$ assuming spherical shape particles. The volume fraction and number density of the PP particles were evaluated from Q2 an $\Delta \rho_{PP}^2 = 45.1 \times 10^{20} \, \text{cm}^{-4}$ (Table A3) in D₂O as $\Phi_{PP} \simeq 2.06 \times 10^{-5}$ and $N_{PP} \simeq 6.9 \times 10^6 \, \text{cm}^{-3}$, respectively. The scattering of particles of such low concentration is too small to be detected in the RO-MC cell. It is 3 and 4 orders of magnitude smaller compared to membrane scattering at Q $\simeq 2 \times 10^{-4} \, \text{Å}^{-1}$ (Fig. 1b). The volume fraction of PP particles is certainly determined, among other things, by the limited volume of the pipe circuit (330 mL) and the fact that we do not drain the concentrate into a separate tank. The relatively small volume of 330 mL was also chosen because of the expensive D₂O. How can feed water be contaminated with PP particles without being in direct contact with the PP nonwoven layer in the RO-MC cell? The PA surface of the membrane in the RO-MC cell must have been contaminated with PP particles before the SANS experiments were started. The contamination could have occurred during manufacturing or during the membrane cleaning procedure described above.

References

- M.E. Williams, A Brief Review of Reverse Osmosis Membrane Technology, https:// www.academia.edu.
- [2] R.W. Baker, Membrane Technology and Applications, Third Edition, John Wiley & Sons Inc., Hoboken, NJ 07030, USA, 2012.
- [3] M. Qasim, M. Badrelzaman, N.N. Darwish, N.A. Darwish, N. Hilal, Reverse osmosis desalination: A State-of-the-Art Review, Desalination 459 (2019) 59–104, https://doi.org/10.1016/j.desal.2019.02.008.
- [4] L. Malaeb, G.M. Ayoub, Reverse osmosis technology for water treatment: State of the art review, Desalination 267 (2011) 1–8, https://doi.org/10.1016/j. doi:10.1016/j.0011
- [5] S.E. Bone, G.G. Steinrück, M.F. Toney, Advanced Characterization in Clean Water Technologies, Joule 4 (2020) 1637–1659, https://doi.org/10.1016/j. ioule 2020 06 020
- [6] V. Pipich, Y.N. Dahdal, H. Rapaport, Y. Kasher, D.S. Oren, Effects of Biological Molecules on Calcium Mineral Formation Associated with Wastewater Desalination as Assessed using Small-Angle Neutron Scattering, Langmuir 29 (2013) 7607–7617, https://doi.org/10.1021/la4001889.
- [7] Y.N. Dahdal, V. Pipich, H. Rapaport, Y. Oren, R. Kasher, D. Schwahn, Small-Angle Neutron Scattering Studies of Mineralization on BSA coated Citrate capped Gold Nano-Particles used as a Model Surface for Membrane Scaling in RO Wastewater Desalination, Langmuir 2014 (30) (2014) 15072–15082, https://doi.org/10.1021/ la502706k.
- [8] Y.N. Dahdal, V. Pipich, H. Rapaport, Y. Oren, R. Kasher, D. Schwahn, Small-Angle Neutron Scattering Studies of Alginate as Biomineralizing Agent and Scale Initiator, Polymer 85 (2016) 77–88, https://doi.org/10.1016/j. polymer 2016 01 012
- [9] A. Heiss, W. Jahnen-Dechent, H. Endo, D. Schwahn, Structural dynamics of a colloidal protein - mineral complex bestowing on calcium phosphate a high solubility in biological fluids, Biointerphases 2 (2007) 16–20, https://doi.org/ 10.1116/1.2714924.
- [10] A. Heiss, V. Pipich, W. Jahnen-Dechent, D. Schwahn, Fetuin-A is a Mineral Carrier Protein: Small Angle Neutron Scattering provides new Insight on Fetuin-A controlled Calcification Inhibition, Biophysical Journal 99 (2010) 3986–3995, https://doi.org/10.1016/j.bpj.2010.10.030.
- [11] V. Pipich, M. Dickmann, H. Frielinghaus, R. Kasher, Ch. Hugenschmidt, W. Petry, Y. Oren, D. Schwahn, Morphology of thin film composite membranes explored by small-angle neutron scattering and positron-annihilation lifetime spectroscopy, Membrane MDPI 10 (2020) 48, https://doi.org/10.3390/membranes10030048.
- [12] V. Pipich, K. Schlenstedt, M. Dickmann, R. Kasher, J. Meier-Haack, Ch. Hugenschmidt, W. Petry, Y. Oren, D. Schwahn, Morphology and porous structure of standalone aromatic polyamide films as used in RO membranes – an

- exploration with SANS, PALS, and SEM, Journal of Membrane Science 573 (2019) 167–176, https://doi.org/10.1016/j.memsci.2018.11.055.
- [13] D. Schwahn, H. Feilbach, Th. Starc, V. Pipich, R. Kasher, Y. Oren, Design and Test of Reverse Osmosis Pressure Cell for in-situ Small-Angle Neutron Scattering Studies, Desalination 405 (2017) 40–50, https://doi.org/10.1016/j. desal.2016.11.026.
- [14] V. Pipich, Th. Starc, J. Buitenhuis, R. Kasher, W. Petry, Y. Oren, D. Schwahn, Silica Fouling in Reverse Osmosis Systems-Operando Small-Angle Neutron Scattering Studies, Membranes (MDPI) 11 (2021) 413, https://doi.org/10.3390/ membranes11060413.
- [15] S. Jamaly, N.N. Darwish, I. Ahmed, S.W. Hasan, A short review on reverse osmosis pretreatment technologies, Desalination 354 (2014) 30–38, https://doi.org/ 10.1016/j.desal.2014.09.017.
- [16] L. Huang, J.R. McCutcheon, Impact of support layer pore size on performance of thin film composite membranes for forward osmosis, Journal of Membrane Science 483 (2015) 25–33, https://doi.org/10.1016/j.memsci.2015.01.025.
- [17] S. Jalal-Al-Din Sharabatia, S. Guclua, D.Y. Erkoc-Ilter, S. Koseoglu-Imera, Y. Z. Unal, I. Menceloglu, I.K. Ozturk, Interfacially polymerized thin-film composite membranes: Impact of support layer pore size on active layer polymerization and seawater desalination performance, Separation and Purification Technology 212 (2019) 438–448, https://doi.org/10.1016/j.seppur.2018.11.047.
- [18] A. Tiraferri, N.Y. Yip, W.A. Phillip, J.D. Schiffman, M. Elimelech, Relating performance of thin-film composite forward osmosis membranes to support layer formation and structure, Journal of Membrane Science 367 (2011) 340–352, https://doi.org/10.1016/j.memsci.2010.11.014.
- [19] A.K. Ghosh, E.M.V. Hoek, Impacts of support membrane structure and chemistry on polyamide-polysulfone interfacial composite membranes, Journal of Membrane Science 336 (2009) 140–148. https://doi:10.1016/j.memsci.2009.03.024.
- [20] Heinz Maier-Leibnitz-Zentrum: https://mlz-garching.de/englisch/instrumentsund-labs.html.
- [21] KWS3: Very small-angle scattering diffractometer with focusing mirror, Journal of large-scale research facilities, 1, A31.
- [22] KWS1: Small-angle scattering diffractometer, Journal of large-scale research facilities, 1, A28.
- [23] J. Barker, J. Moyer, St. Kline, G. Jensen, J. Cook, C. Gagnon, E. Kelley, J.Ph. Chabot, N. Maliszewskyj, C. Parikh, W. Chen, R.P. Murphya, Ch. Glinka, The very small angle neutron scattering instrument at the National Institute of Standards and Technology, J. Appl. Cryst. 55 (2022) 271–283. https://doi.org/10.1107/S1600576722000826.
- [24] D. Richter, D. Schwahn, in: Neutron Scattering in Polymers Structure-Properties and Characterization, in Macromolecular Engineering: from Precise Synthesis to Macroscopic Materials and Applications, 2nd ed.;, (WILEY-VCH GmbH, Weinheim, Germany, 2022, pp. 1–38, https://doi.org/10.1002/9783527815562.mme0044.
- [25] Membranes were received from Alfa Laval Mid Europe GmbH, Wilhelm-Bergner-Straße 7, DE-21509 Glinde (Germany).

- [26] V. Pipich, D. Schwahn, Densification of Supercritical Carbon Dioxide (CO₂) accompanied by Droplet Formation when passing the Widom Line, Phys. Rev. Lett. 120 (2018) 145701, https://doi.org/10.1103/PhysRevLett.120.145701.
- [27] V. Pipich, D. Schwahn, Polymorphic phase transition in liquid and supercritical carbon dioxide, natureresearch, Scientific Reports 2020 (10) (2020) 11861, https://doi.org/10.1038/s41598-020-68451-y.
- [28] R.J. Roe, Methods of X-ray and neutron scattering in polymer science, University Press, Oxford, 2000.
- [29] G. Porod, General Theory, in: O. Glatter, O. Kratky (Eds.), Small Angle X-Ray Scattering, Academic Press, London, Great Britain, 1982, pp. 17–51.
- [30] J. Palacios, D. Schwahn, H. Rauch, High Angular Resolution Neutron Transmission Measurements - A Proposed Nondestructive Material Testing Method, NDT International 14 (1981) 189–193, https://doi.org/10.1016/0308-9126(81)90005-5
- [31] E.M. Anitas, Small-Angle Scattering from Fractals: Differentiating between Various Types of Structures, Symmetry MDPI 12 (2020) 65, https://doi.org/10.3390/ sym12010065.
- [32] C.J. Glinka, Incoherent Neutron Scattering from Multi-element Materials, J. Appl. Cryst. 44 (2011) 618–624, https://doi.org/10.1107/S0021889811008223.
- [33] V.F. Sears, Neutron scattering length and cross section, Neutron News 3 (1992) 26–37, https://doi.org/10.1080/10448639208218770.
- [34] F. Foglia, B. Frick, M. Nania, A.G. Livingston, J.T. Cabral, Multimodal confined water dynamics in reverse osmosis polyamide membranes, Nature Communications 13 (2022) 2809, https://doi.org/10.1038/s41467-022-30555-6.
- [35] R.E. Ghosh, A.R. Rennie, Assessment of detector calibration materials for SANS, J. Appl. Cryst. 32 (1999) 1157–1167, https://doi.org/10.1107/ S0021889899009991
- [36] X. Song, J.W. Smith, J. Kim, N.J. Zaluzec, W. Chen, H. An, J.M. Dennison, D. G. Cahill, M.A. Kulzick, Q. Chen, Unravelling the morphology-function relationships of polyamide membranes using quantitative electron tomography, ACS Appl. Mater. Interfaces 11 (2019) 8517–8526, https://doi.org/10.1021/acsami.8b20826.
- [37] M.E. Yakavalangi, S. Rimaz, V. Vatanpour, Effect of surface properties of polysulfone support on the performance of thin film composite polyamide reverse osmosis membranes, J. Appl. Polym. Sci. 134 (2017) 44444, https://doi.org/ 10.1002/app.44444.
- [38] T. Melin, R. Rautenbach, Membranverfahren, Grundlagen der Modul- und Anlagenauslegung, 3. Auflage, Springer-Verlag, Berlin Heidelberg, 2007.

- [39] V. Freger, Nanoscale Heterogeneity of Polyamide Membranes Formed by Interfacial Polymerization, Langmuir 19 (2003) 4791–4797.
- [40] H.F. Ridgway, J. Orbell, S. Gray, Molecular simulations of polyamide membrane materials used in desalination and water reuse applications: Recent developments and future prospects, Journal of Membrane Science 524 (2017) 436–448.
- [41] G.L. Squires, Introduction to the theory of Thermal Neutron Scattering, Cambridge University Press, Cambridge, Great Britain, 1978.
- [42] M. Bée, Quasielastic Neutron Scattering, Principles and Applications in Solid State Chemistry, Biology and Materials Science, Adam Hilger, Bristol, Great Britain, 1988.
- [43] F. Pacheco, R. Sougrat, M. Reinhard, J.O. Leckie, I. Pinnau, 3D visualization of the internal nanostructure of polyamide thin films in RO membranes, Journal of Membrane Science 501 (2016) 33–44.
- [44] L. Lin, R. Lopez, G.Z. Ramon, O. Coronell, Investigating the void structure of the polyamide active layers of thin-film composite membranes, Journal of Membrane Science 497 (2016) 365–376.
- [45] T.E. Culp Y. Shen, M. Geitner, M. Paul, A. Roy, M.J. Behr, St. Rosenberg, J. Gu, M. Kumar, E.D. Gomez, Electron tomography reveals details of the internal microstructure of desalination membranes, PNAS 115 (2018) 8694–8699.
- [46] X. Song, J.W. Smith, J. Kim, N.J. Zaluzec, W. Chen, H. An, J.M. Dennison, D. G. Cahill, M.A. Kulzick, Q. Chen, Unraveling the Morphology—Function Relationships of Polyamide Membranes Using Quantitative Electron Tomography, ACS Appl. Mater. Interfaces 11 (2019) 8517–8526.
- [47] Z. Steiner, H. Rapaport, Y. Oren, R. Kasher, Effect of surface-exposed chemical groups on calcium-phosphate mineralization in water-treatment system, Environ. Sci. Technol. 44 (2010) 7937–7943, https://doi.org/10.1021/es101773t.
- [48] B. Alefeld, D. Schwahn, T. Springer, New developments of small angle neutron scattering instruments with focusing, Nuclear Instruments and Methods in Physics Research Section A 274 (1989) 210–216, https://doi.org/10.1016/0168-9002(89) 90382-3.
- [49] G.D. Wignall, F.S. Bates, Absolute calibration of small-angle neutron scattering data, J. Appl. Cryst. 20 (1987) 28–40, https://doi.org/10.1107/ S0021880887087181
- [50] F.R. Spellman, Reverse Osmosis, A Guide for the Nonengineering Professional, CRC Press, Taylor & Francis Group, Boca Raton, Florida, USA (2016), https://doi.org/ 10.1201/b18732
- [51] G. Beaucage, G., Approximations leading to a unified exponential power-law approach to small-angle scattering, J. Appl. Cryst. 28 (1995) 717–728.